

# Hydrodynamical models of cometary H II regions

H. G. Steggle<sup>\*</sup>, M. G. Hoare<sup>\*</sup> and J. M. Pittard<sup>\*</sup>

*School of Physics and Astronomy, University of Leeds, Woodhouse Lane, Leeds LS2 9JT*

Accepted 2016 December 23. Received 2016 December 22; in original form 2016 August 23

## ABSTRACT

We have modelled the evolution of cometary H II regions produced by zero-age main-sequence stars of O and B spectral types, which are driving strong winds and are born off-centre from spherically symmetric cores with power-law ( $\alpha = 2$ ) density slopes. A model parameter grid was produced that spans stellar mass, age and core density. Exploring this parameter space, we investigated limb-brightening, a feature commonly seen in cometary H II regions. We found that stars with mass  $M_{\star} \geq 12 M_{\odot}$  produce this feature. Our models have a cavity bounded by a contact discontinuity separating hot shocked wind and ionized ambient gas that is similar in size to the surrounding H II region. Because of early pressure confinement, we did not see shocks outside of the contact discontinuity for stars with  $M_{\star} \leq 40 M_{\odot}$ , but the cavities were found to continue to grow. The cavity size in each model plateaus as the H II region stagnates. The spectral energy distributions of our models are similar to those from identical stars evolving in uniform density fields. The turn-over frequency is slightly lower in our power-law models as a result of a higher proportion of low-density gas covered by the H II regions.

**Key words:** hydrodynamics – radiative transfer – stars: evolution – stars: massive – stars: winds, outflows – H II regions.

## 1 INTRODUCTION

Massive stars ( $M_{\star} > 8 M_{\odot}$ ) are an important component of the Universe. They are the main sources of stellar feedback that influences the structure, evolution and chemical composition of a galaxy. High-mass stars are born in dense parts of the interstellar medium (ISM), erupting with outflows and radiatively driven winds that contribute to the destruction of the natal cloud. Extreme ultraviolet radiation is emitted from high-mass stars, which ionizes and heats the surrounding gas. This produces an over-pressure that drives a shock into the ambient medium, sweeping gas into a shell that ultimately disperses the parent molecular cloud and may also trigger further star formation (Hoare et al. 2007). The optical and near-infrared emission from such stars is not able to penetrate the natal clouds as a result of high column densities of dust. Radio free-free emission can, however, be seen right across the Galaxy (Churchwell 2002). At wavelengths in the far-infrared, emission coming from warm dust re-emitting the stellar radiation can also be observed from ionized nebulae (Cesaroni et al. 2015).

How high-mass stars are formed is still poorly understood. They have short main-sequence lifetimes ( $\lesssim 10^8$  yr) which, along with their relatively low formation rates, indicates that only a small proportion ( $\simeq 10^{-6}$ ) of stars in the galaxy have high masses. The scarcity of observational data is a significant problem for the testing

of theoretical models; some important phases of evolution pass very quickly. The youngest massive stars, however, are associated with UCH II regions, a phase that lasts longer than expected (Wood & Churchwell 1989a). UCH II regions were defined by Wood & Churchwell (1989a) as photo-ionized nebulae with diameters  $\lesssim 0.1$  pc, electron number densities  $\gtrsim 10^4$  cm $^{-3}$  and emission measures  $\gtrsim 10^7$  pc cm $^{-6}$  that have not yet expanded out of their natal molecular cloud. The observed ionization from such stars indicates that the ionizing photon emission rates lie approximately between  $10^{44}$  and  $10^{49}$  s $^{-1}$  corresponding to zero-age main-sequence (ZAMS) stars with spectral types B2–O5. Wood & Churchwell (1989b) estimated the lifetime of UCH II regions ( $\sim 4 \times 10^5$  yr) using the fraction of main-sequence stars observed in the UCH II phase and an adopted value for the main-sequence lifetime ( $\sim 2.4 \times 10^6$  yr). This lifetime is an order of magnitude longer than that predicted by simple Strömgren sphere expansion ( $\sim 4 \times 10^4$  yr).

UCH II regions are interesting to study as they may provide a lot of information about the early life of massive stars including their properties and, because of the limited number of observed morphological classes, their environments. The survey of Wood & Churchwell (1989a) included classifications of UCH II regions into morphological types: cometary ( $\sim 20$  per cent), core-halo ( $\sim 16$  per cent), shell ( $\sim 4$  per cent), irregular or multiple peaked structures ( $\sim 17$  per cent) and spherical and unresolved ( $\sim 43$  per cent). Kurtz, Churchwell & Wood (1994) made radio-continuum observations of 75 UCH II regions for which the proportions of morphological types agree remarkably well with those in Wood & Churchwell (1989a). Observed at higher spatial resolution, some apparently

<sup>\*</sup> E-mail: hgsteggles@gmail.com (HGS); M.G.Hoare@leeds.ac.uk (MGH); J.M.Pittard@leeds.ac.uk (JMP)

spherical morphologies uncover more ordered morphologies (Felli, Churchwell & Massi 1984). The radio continuum survey of UCH II regions by Walsh et al. (1998) found that most sources were either cometary or irregular (ignoring the unresolved sources). De Pree et al. (2005) revised the morphological scheme by adding the bipolar classification and removing the core-halo morphology. The latter was due to the fact that essentially all UCH II regions were observed to be associated with large-scale diffuse emission that could be separated from the compact cores. The proportions of the morphologies in this survey compare well with the surveys of Wood & Churchwell (1989a) and Kurtz et al. (1994) except that 28 per cent of sources were classed as shell-like. Hoare et al. (2007) reviewed the different morphological surveys and noted that a lot of morphologies classified as shell-like could also be classified as cometary.

As UCH II regions have had little time to significantly alter their natal environments, the morphologies that arise are thought to reflect the ambient density field. Cometary types, in particular, are interesting to study and to test numerical models against, because they have a highly regular shape and can overcome the lifetime problem. In the past, there were three major models that aimed to explain how UCH II regions form cometary shapes: the champagne flow model (Israel 1978), the bow shock model (Reid & Ho 1985; Mac Low et al. 1991; van Buren & Mac Low 1992) and clumpy/mass-loading models (Dyson, Williams & Redman 1995; Redman, Williams & Dyson 1996; Williams, Dyson & Redman 1996). A more recent idea says that the situation is probably best described by a combination of these (i.e. hybrid models; Arthur & Hoare 2006).

Cometary H II regions are mostly observed at the edge of molecular clouds. Along with the shape, this is the reason they were first called ‘blisters’ (Israel 1978). This led to the champagne flow model, a modification of the simple Strömgen solution in which the ionizing star lies in an inhomogeneous (not a uniform) density field. Early modelling by Tenorio-Tagle (1979), Whitworth (1979), Bodenheimer, Tenorio-Tagle & Yorke (1979), Bedijn & Tenorio-Tagle (1981) and Tenorio-Tagle, Yorke & Bodenheimer (1979) included discontinuities in density separating molecular clouds with the ISM. Bodenheimer et al. (1979) found that once the ionized gas reaches the edge of the dense cloud, it accelerates up to  $\sim 30$  km  $s^{-1}$ . More realistically, Icke (1979a,b), Icke, Gatley & Israel (1980) and Yorke, Tenorio-Tagle & Bodenheimer (1983) modelled stars in density gradients, clearly reproducing cometary morphologies and predicting double spectral line profiles corresponding to a velocity splitting of up to 50 km  $s^{-1}$  along the symmetry axis. Henney, Arthur & García-Díaz (2005) carried out simulations of the photo-evaporation of a cloud with large-scale density gradients. They showed that an ionized flow is set up that has a transient phase with duration  $\sim 10^4$  yr, which then becomes approximately stationary with respect to the ionization front (the quasi-stationary phase) for a large part of its evolution.

Real H II regions cannot be explained entirely in terms of a density gradient. Not only does the champagne model fail to exhibit limb-brightened morphologies, but also the lifetime problem is not solved due to the unconstrained expansion of the ionization front. It also does not take into account the fact that OB stars drive stellar winds that can significantly affect the dynamics of nearby gas.

If an ionizing star moves supersonically with respect to a uniform density field, then the strong stellar wind driven by that star balances the ram pressure produced by the ambient flow, forming a bow shock ahead of the star. This model was introduced by van Buren et al. (1990) as an alternative explanation of cometary H II regions and later analysed numerically by van Buren & Mac Low (1992). They

found that behind the bow shock, neutral material is swept up into a very dense, thin shell that traps the expanding ionization front. This was a good result for the bow shock model as it was known that a confining mechanism was necessary to solve the lifetime problem. Limb-brightening was also found to occur in this model and can be explained as ionized gas that has been compressed by the stellar wind into a thin shell, flowing around the stellar wind cavity. The bow shock model was attractive because the size and shape compared well with observed cometary UCH II regions and it explained velocity gradients commonly seen at the head of cometary.

Zhu et al. (2015) simulated the evolution of cometary H II regions in bow shock and champagne flow models and analysed the resulting [Ne II] 12.81  $\mu\text{m}$  and H<sub>2</sub>S(2) line profiles. They discovered that the two models can be distinguished using these lines.

Both the bow shock model and the champagne flow model have been found to be inadequate in explaining the recombination line velocity structures of cometary H II regions. Lumsden & Hoare (1996) investigated the validity of both models in reproducing the velocity structure of the cometary UCH II region G29.96–0.02 and found that individually they poorly describe the object. Gaume, Fey & Claussen (1994) suggested that by including stellar winds and non-uniform ambient density fields, more realistic models could be made.

Franco et al. (2007) studied the evolution of H II regions moving from the centre to the edge of structured molecular clouds with Gaussian cores surrounded by power-law ( $\rho \propto r^{-2}$  and  $\rho \propto r^{-3}$ ) haloes. They found that UCH II regions remain pressure-confined while they are inside the core but evolve into extended H II regions as they move into lower-density regions of the cloud. A variety of hybrid models were investigated by Arthur & Hoare (2006) including champagne flow plus stellar wind and a combination of bow shock and champagne flow models in which the density gradient and the strength of the stellar wind were varied. With the inclusion of a stellar wind, it was discovered that it is possible for a champagne flow to produce limb-brightened morphologies. This is because the stellar wind creates a dense shell that acts as a barrier to photo-evaporated flows, which divert around it. Arthur & Hoare (2006) found that for simple bow shock models the linewidths are highest ahead of the massive star, and for simple champagne flow models the widths are highest in the tail. They found that for hybrid models, a slow moving star in a steep density gradient has larger velocity widths toward the tail, but a fast moving star in shallow density gradients has its largest velocity widths nearer the star. Making sure to remove the effect of any cloud velocity, a hybrid model that matches the line data of a cometary H II region could be used to gather information about the density structure of the natal cloud.

Three-dimensional simulations of H II regions expanding off-centre in turbulent, self-gravitating power-law cores were run by Mac Low et al. (2007). They found that the expanding H II regions were roughly spherical and noted that this is consistent with the analytical results of Korycansky (1992). These results were also confirmed by Arthur (2007) who performed similar simulations for  $r^{-2}$  and  $r^{-3}$  power-law density cores.

New Galactic plane surveys are revisiting the lifetime problem and providing large, well-selected samples. The Galaxy-wide Red MSX Source (RMS) survey found  $\sim 900$  mid-infrared bright compact H II regions (Lumsden et al. 2013). Mottram et al. (2011) used the results of this survey and determined the lifetime of the compact H II phase to be 300 kyr or  $\sim 3$ –10 per cent of the source’s main-sequence lifetime. Davies et al. (2011) simulated the RMS results using a particular Galactic gas distribution and

different accretion models and compared these with the luminosity distribution of the RMS survey. In this work, each ionizing star in the Galaxy was assumed to be producing H II regions in a uniform density medium and not blowing a stellar wind (i.e. simple Strömgen expansion).

The aim of the current paper is to produce a grid of more realistic UCH II regions to include in the galaxy model of Davies et al. (2011) by simulating cometary H II regions. We explore a parameter space spanning stellar mass, the density of the stellar environment and the age of the star and we note the behaviour of some observables across this space. In a subsequent paper, we will use this model grid to provide more realistic H II region sizes and fluxes in an improved galaxy model that will be tested against the Co-Ordinated Radio ‘N’ Infrared Survey for High-mass star formation (CORNISH) survey (Hoare et al. 2012; Purcell et al. 2013). The CORNISH survey is an arcsec-resolution 5-GHz radio survey of the northern half of the GLIMPSE region ( $10 \text{ deg} < l < 65 \text{ deg}$ ,  $|b| < 1 \text{ deg}$ ) for compact ionized sources. With such a large unbiased sample of UCH II regions ( $\sim 240$ ), it will be possible to test the models in the context of high-mass star formation on the Galactic scale.

In Section 2 we introduce the numerical scheme and describe the models we simulated. The results of the simulations are presented in Section 3 and we discuss the behaviour of the hot stellar wind region, the ionization front, the emission measures and the spectral indices when stellar mass, age and cloud density are varied. We conclude the paper in Section 4 where we summarize our findings.

## 2 THE MODEL

### 2.1 Numerical scheme

Our simulations use The Operator-split Radiation, Cooling, Hydrocode (TORCH), which is a three-dimensional Eulerian fixed grid fluid dynamics code (code tests are given in Appendix A). Three coupled physics problems (hydrodynamics, radiative transfer and heating/cooling) are integrated separately and the result of each is combined to update the solution at each step using the Strang splitting scheme (Strang 1968).

The fluid dynamics was solved on a two-dimensional axisymmetric grid (Falle 1991) using a rotated-hybrid Harten–Lax–van Leer Contact (HLLC)–Harten–Lax–van Leer (HLL) Riemann solver (see Appendix B) to calculate numerical fluxes on each inter-cell boundary. Left and right Riemann states are interpolated via a Monotonic Upstream-centred Scheme for Conservation Laws (MUSCL) scheme (van Leer 1979) that uses the van Albada slope limiter (van Albada, van Leer & Roberts 1982). Rotated-hybrid Riemann solvers automatically apply fewer wave solvers normal to shocks (the HLL solver in this code) in order to eliminate carbuncle instabilities. These solvers are very robust and come with an acceptable drop in performance. The minimum and maximum signal velocities in the HLLC solver are approximated as the minimum and maximum eigenvalues of the Roe matrix (Roe 1981). The hydrodynamics scheme is second-order accurate in time and space.

The transfer of ionizing radiation is calculated using the  $C^2$ –Ray method by Mellema et al. (2006). At each step, the optical depth to each cell is traced via the method of short-characteristics. In this method, the optical depth to the target cell is a weighted average of optical depths in neighbouring cells that lie between the target cell and the cell containing the ionizing source. The ionization fraction in each cell is implicitly solved before the cell’s optical depth can be used in calculations for other cells (which constrains the order in which the cells are iterated over).

Heating from different types of radiation and cooling due to collisional excitation and recombination is calculated using the approximate functions in Henney et al. (2009).

The governing hydrodynamic equations are:

conservation of mass,

$$\frac{\partial \rho}{\partial t} + \nabla \cdot (\rho \mathbf{u}) = \dot{\rho}_w(\mathbf{r}); \quad (1)$$

conservation of momentum,

$$\frac{\partial (\rho \mathbf{u})}{\partial t} + \nabla \cdot (\rho \mathbf{u} \otimes \mathbf{u}) + \nabla p = \mathbf{0}; \quad (2)$$

and conservation of energy,

$$\frac{\partial e}{\partial t} + \nabla \cdot [\mathbf{u}(e + p)] = H - C + \dot{e}_w(\mathbf{r}). \quad (3)$$

Here,  $\rho$  is the gas density,  $\mathbf{u}$  is the fluid velocity,  $p$  is the thermal pressure,  $e = 1/(\gamma - 1)p + (1/2)\rho u^2$  is the total energy density with  $\gamma = 5/3$ ,  $H$  and  $C$  are, respectively, the heating and cooling rates due to atomic/molecular transitions,  $\dot{e}_w(\mathbf{r})$  is the injection rate of stellar wind energy density and  $\dot{\rho}_w(\mathbf{r})$  is the injection rate of wind material density as a function of position.

We also have equations describing the advection of the hydrogen ionization fraction,

$$\frac{\partial (f \rho)}{\partial t} + \nabla \cdot (f \rho \mathbf{u}) = \dot{\rho}_w(\mathbf{r}), \quad (4)$$

and the rate of hydrogen ionizations and recombinations,

$$\frac{df}{dt} = (1 - f)(\Gamma + n_e C_H) - f n_e \alpha_H, \quad (5)$$

where  $f$  is the fraction of hydrogen that is ionized,  $n_e$  is the electron number density,  $\Gamma$  is the photo-ionization rate,  $C_H$  is the collisional ionization coefficient and  $\alpha_H$  is the recombination coefficient of hydrogen.

Models were simulated on a numerical grid with square cells that have equal side lengths. The resolution of each grid is given in Table 1 along with the physical dimensions. On the edges of the simulation domain, we applied Dirichlet boundary conditions. Specifically, we applied reflective conditions on the boundary at  $r = 0$  and outflow conditions on the other boundaries.

### 2.2 The star’s environment

Our model environment has the same density structure as Model F in Arthur & Hoare (2006). Stars in these models are off-centre in a spherically symmetric density distribution at a distance of 0.35 pc from the cloud centre. The density is given by

$$\rho = \rho_0 \left[ 1 + \left( \frac{r}{r_c} \right)^2 \right]^{(-\alpha)/2}, \quad (6)$$

where  $r$  is the distance from the cloud centre,  $r_c = 0.01 \text{ pc}$  is the cloud core radius,  $\rho_0$  is the density at the cloud centre and the power-law index  $\alpha$  parametrizes the dependence on  $r$  when  $r \gg r_c$ . The density at the star’s position is then given by

$$\rho_* = \rho_0 \left[ 1 + \left( \frac{r_{sc}}{r_c} \right)^2 \right]^{(-\alpha)/2}, \quad (7)$$

where  $r_{sc} = 0.35 \text{ pc}$  is the distance of the star from the cloud centre, so that  $\rho_* = (1/1226)\rho_0$ .

The power-law index,  $\alpha$ , has been inferred using a number of different techniques, leading to a wide range of values in the literature.

**Table 1.** The grid of parameters used for the models: stellar mass,  $M_*$ ; the number density,  $n_*$ , of the cloud of hydrogen gas at the position of the star at the start of the simulation; the number of numerical grid cells along the radial axis,  $N_r$ ; the number of numerical grid cells along the polar axis,  $N_z$ ; and the physical extent of the numerical grid along the radial direction,  $L_r$ . The other columns are calculated values for each model including: the Strömgren radius to star-cloud distance ratio,  $y_{sc}$ ; the wind start time,  $t_{start}$ ; and the cooling time in the injection region,  $t_{cool}$ .

$M_*$ ( $M_\odot$ )	$n_*$ ( $\text{cm}^{-3}$ )	$N_r$	$N_z$	$L_r$ (pc)	$y_{sc}$	$R_{inj}$ (pc)	$t_{start}$ (kyr)	$t_{cool}$ (kyr)
6	$8.00 \times 10^3$	150	400	0.10	0.006	0.007	0.257	$5.503 \times 10^3$
9	$8.00 \times 10^3$	150	300	0.15	0.018	0.010	0.357	$7.468 \times 10^4$
12	$8.00 \times 10^3$	150	200	0.50	0.047	0.033	1.002	$9.027 \times 10^3$
15	$8.00 \times 10^3$	150	200	0.50	0.102	0.033	0.172	$8.634 \times 10^3$
20	$8.00 \times 10^3$	150	200	0.50	0.214	0.033	0.026	$1.703 \times 10^4$
30	$8.00 \times 10^3$	150	200	1.00	0.363	0.067	0.029	$1.475 \times 10^4$
40	$8.00 \times 10^3$	150	200	1.50	0.494	0.100	0.025	$1.069 \times 10^4$
70	$8.00 \times 10^3$	150	200	3.00	0.681	0.200	0.035	$1.086 \times 10^4$
120	$8.00 \times 10^3$	150	200	9.00	0.858	0.601	0.243	$1.164 \times 10^4$
6	$1.60 \times 10^4$	150	300	0.06	0.004	0.004	0.111	$2.577 \times 10^3$
9	$1.60 \times 10^4$	150	300	0.15	0.011	0.010	0.715	$2.879 \times 10^2$
12	$1.60 \times 10^4$	150	250	0.25	0.029	0.017	0.250	$3.539 \times 10^4$
15	$1.60 \times 10^4$	150	200	0.50	0.064	0.033	0.344	$1.425 \times 10^4$
20	$1.60 \times 10^4$	150	200	0.50	0.135	0.033	0.052	$1.579 \times 10^4$
30	$1.60 \times 10^4$	150	200	0.50	0.229	0.033	0.007	$4.868 \times 10^3$
40	$1.60 \times 10^4$	150	200	1.00	0.311	0.067	0.015	$5.620 \times 10^3$
70	$1.60 \times 10^4$	150	200	2.00	0.429	0.134	0.021	$5.391 \times 10^3$
120	$1.60 \times 10^4$	150	200	5.00	0.540	0.334	0.083	$8.106 \times 10^3$
6	$3.20 \times 10^4$	150	300	0.05	0.002	0.003	0.128	$1.290 \times 10^3$
9	$3.20 \times 10^4$	150	400	0.08	0.007	0.005	0.217	$2.778 \times 10^4$
12	$3.20 \times 10^4$	150	300	0.20	0.019	0.013	0.256	$2.828 \times 10^4$
15	$3.20 \times 10^4$	150	200	0.50	0.040	0.033	0.688	$3.957 \times 10^3$
20	$3.20 \times 10^4$	150	200	0.50	0.085	0.033	0.103	$1.449 \times 10^4$
30	$3.20 \times 10^4$	150	200	0.50	0.144	0.033	0.015	$4.869 \times 10^3$
40	$3.20 \times 10^4$	150	200	1.00	0.196	0.067	0.030	$1.559 \times 10^3$
70	$3.20 \times 10^4$	150	200	3.00	0.270	0.200	0.139	$1.052 \times 10^4$
120	$3.20 \times 10^4$	150	200	5.00	0.340	0.334	0.167	$2.381 \times 10^3$
6	$6.40 \times 10^4$	150	300	0.03	0.001	0.002	0.055	$7.395 \times 10^2$
9	$6.40 \times 10^4$	150	300	0.05	0.004	0.003	0.106	$9.792 \times 10^2$
12	$6.40 \times 10^4$	150	200	0.20	0.012	0.013	0.513	$1.746 \times 10^4$
15	$6.40 \times 10^4$	150	300	0.25	0.025	0.017	0.172	$1.477 \times 10^4$
20	$6.40 \times 10^4$	150	200	0.50	0.053	0.033	0.207	$1.139 \times 10^4$
30	$6.40 \times 10^4$	150	200	0.50	0.091	0.033	0.029	$4.873 \times 10^3$
40	$6.40 \times 10^4$	150	200	0.50	0.123	0.033	0.007	$1.559 \times 10^3$
70	$6.40 \times 10^4$	150	200	0.50	0.170	0.033	0.001	$9.800 \times 10^2$
120	$6.40 \times 10^4$	150	200	2.00	0.214	0.134	0.021	$1.565 \times 10^3$
6	$1.28 \times 10^5$	150	300	0.03	0.001	0.002	0.064	$3.734 \times 10^2$
9	$1.28 \times 10^5$	150	300	0.04	0.003	0.003	0.108	$7.410 \times 10^3$
12	$1.28 \times 10^5$	150	300	0.10	0.007	0.007	0.128	$4.389 \times 10^3$
15	$1.28 \times 10^5$	150	300	0.20	0.016	0.013	0.176	$9.584 \times 10^3$
20	$1.28 \times 10^5$	150	200	0.50	0.034	0.033	0.414	$5.538 \times 10^3$
30	$1.28 \times 10^5$	150	200	0.50	0.057	0.033	0.058	$4.829 \times 10^3$
40	$1.28 \times 10^5$	150	200	0.50	0.078	0.033	0.015	$1.559 \times 10^3$
70	$1.28 \times 10^5$	150	200	0.50	0.107	0.033	0.003	$3.986 \times 10^2$
120	$1.28 \times 10^5$	150	200	0.50	0.135	0.033	0.001	$4.178 \times 10^2$

Hatchell & van der Tak (2003) found indices between 1.25 and 2.25. Five of the seven dark cloud envelopes that were investigated by Arquilla & Goldsmith (1985) were best characterized by an index of  $\alpha \simeq 2$ . A range of 1.0–1.5 was found by van der Tak et al. (2000). Pirogov (2009) found an index of  $\alpha = 1.6 \pm 0.3$  that falls more steeply in the outer layers of the dense core. For the current work, a value of  $\alpha = 2$  was adopted.

The initial pressure in a cloud of constant temperature will have the same structure as the density field. Without gravity, gas will move down the pressure gradient leading to bulk motion that can interfere with the dynamics of the star’s stellar wind and ionization field, especially over the period of 200 kyr each of the simulations

here run for. Instead the pressure of the environment was taken to be uniform such that lower temperatures occur towards the cloud core, and higher temperatures occur away from it (the temperature at the position of the star was 300 K).

### 2.3 Parameters

Using this model environment, we explored key parameters, namely the cloud density at the position of the star and the mass of the ZAMS star. Values for these are given in Table 1. In Table 2, we give the stellar wind parameters, mass-loss rate and terminal velocity (see Table 2), that were calculated using the predictions of

**Table 2.** The stellar parameters used for the models. In order, the columns show: stellar mass,  $M_*$ ; effective temperature,  $T_{\text{eff}}$ ; stellar radius,  $R_*$ ; luminosity,  $L_*$ ; Lyman continuum flux,  $Q_{\text{Ly}\alpha}$ ; the mechanical luminosity of the wind,  $\mathcal{L}$ ; mass-loss rate,  $\dot{M}$ ; the free-flowing wind speed,  $v_\infty$ .

$M_*$ ( $M_\odot$ )	$T_{\text{eff}}$ (K)	$R_*$ ( $R_\odot$ )	$\log_{10}(L_*)$ ( $L_\odot$ )	$\log_{10}(Q_{\text{Ly}\alpha})$ ( $\text{s}^{-1}$ )	$\mathcal{L}$ ( $\text{erg s}^{-1}$ )	$\dot{M}$ ( $M_\odot \text{ yr}^{-1}$ )	$v_\infty$ ( $\text{km s}^{-1}$ )
6	19 000	3.00	3.01	43.33	$5.38 \times 10^{31}$	$1.33 \times 10^{-10}$	$1.13 \times 10^3$
9	22 895	3.90	3.57	44.76	$1.30 \times 10^{32}$	$6.95 \times 10^{-11}$	$2.43 \times 10^3$
12	26 743	4.50	3.96	46.02	$1.72 \times 10^{33}$	$8.03 \times 10^{-10}$	$2.60 \times 10^3$
15	29 783	5.10	4.26	47.03	$1.00 \times 10^{34}$	$4.30 \times 10^{-9}$	$2.71 \times 10^3$
20	33 824	6.00	4.61	48.00	$6.67 \times 10^{34}$	$2.57 \times 10^{-8}$	$2.86 \times 10^3$
30	38 670	7.30	5.02	48.69	$4.73 \times 10^{35}$	$1.54 \times 10^{-7}$	$3.11 \times 10^3$
40	42 610	8.70	5.34	49.09	$1.86 \times 10^{36}$	$5.74 \times 10^{-7}$	$3.20 \times 10^3$
70	47 662	12.00	5.81	49.51	$1.07 \times 10^{37}$	$2.90 \times 10^{-6}$	$3.41 \times 10^3$
120	50 853	17.10	6.23	49.81	$4.13 \times 10^{37}$	$1.11 \times 10^{-5}$	$3.42 \times 10^3$

Vink, de Koter & Lamers (2001). These depend on the metallicity (which was assumed to be solar) and also the effective temperature and luminosity of the star. We took values for these (for certain stellar masses) from Davies et al. (2011), which were calculated using the hydrostatic models of Meynet & Maeder (2000). For the same masses, Lyman continuum fluxes were also taken from Davies et al. (2011) who used calculations from Martins, Schaerer & Hillier (2005) and Lanz & Hubeny (2007). Effective temperature, luminosity and Lyman continuum flux depend only on stellar mass; hence, this is the only free parameter describing the star.

## 2.4 Stellar winds

Vink et al. (2001) determined relations for mass-loss rates of O and B stars for a range of metallicities by using a Monte Carlo radiative transfer method (Vink, de Koter & Lamers 1999; Vink, de Koter & Lamers 2000) on model atmospheres produced by the improved Sobolev approximation code (de Koter, Schmutz & Lamers 1993; de Koter, Heap & Hubeny 1997). This method allowed them to find the radiative momentum transferred to the wind via photon absorptions and scatterings. Self-consistent solutions (i.e. models for which the radiative momentum was equal to the wind momentum of the model atmosphere) were then used to find mass-loss rates. Strictly speaking, the model of Vink et al. (2000) is applicable in the range  $15 \leq M_* \leq 120 M_\odot$ ; we are assuming the authors' results can be extended to predict stellar wind parameters for our model stars with  $M_* < 15 M_\odot$ .

Mass-loss rates and terminal velocities were calculated for each of our model stars using the values in Table 2 and these are plotted in Figs 1 and 2, respectively. As can be seen in the table, the mass injection rate increases for higher mass stars except between 6 and  $9 M_\odot$  where there is a decrease. This is due to the bi-stability jump; the star with  $M_* = 6 M_\odot$  is the only one that lies on the cold side of the bi-stability jump where Fe IV recombines to Fe III, an efficient line driver.

In order to simulate the effects of a stellar wind, we use the thermal energy injection method developed by Chevalier & Clegg (1985), which has also been used by Comeron (1997) and Arthur & Hoare (2006). Because of the resolution of the numerical grid used to simulate our models, we were unable to define a free flowing wind region around the star (as in Rozyczka 1985) that is sufficiently resolved (seed instabilities of low-resolution regions that grow enough to render the simulation results unphysical). The stellar wind power is mostly converted to thermal energy at the reverse shock (Castor, McCray & Weaver 1975) so we do not need to reproduce the

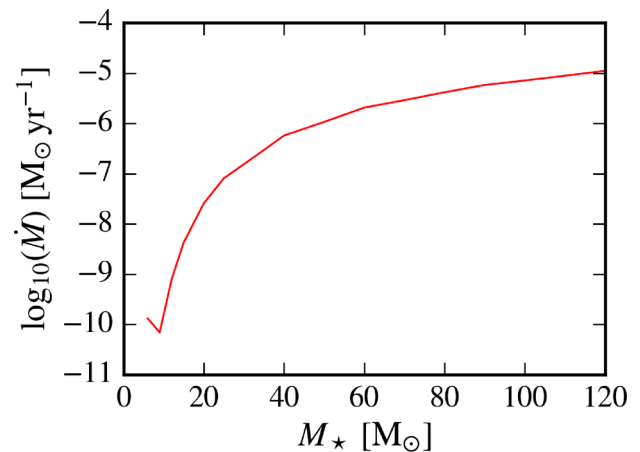


**Figure 1.** The mass-loss rate of stars plotted against stellar mass.

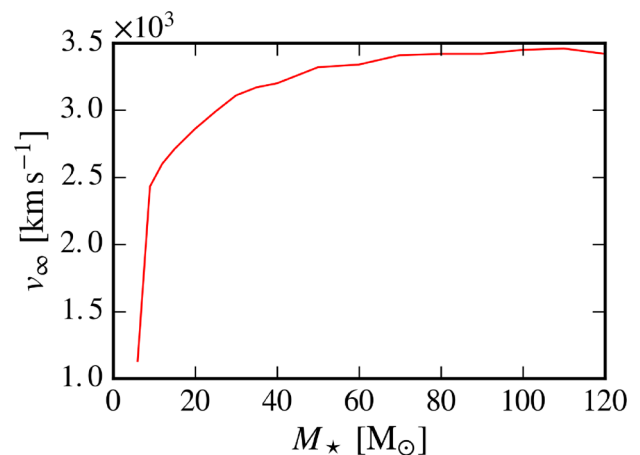


**Figure 2.** The terminal velocity of stellar winds plotted against the driving star's mass.

structure of the unshocked wind region. Instead, we can inject the wind luminosity as a rate of mass,  $\dot{M}$ , and energy,  $(1/2)\dot{M}v_\infty^2$ , into the shocked wind region as it is this power that determines the evolution and structure of the bubble (Weaver et al. 1977). To ensure that the gas in the injection region of our models is adiabatic, the gas is not cooled within the injection region in our simulations.

This method also leads to a shocked stellar wind region with the correct temperature. Inside the injection region, the temperature

is set by the energy injected per unit mass ( $\dot{E}/\dot{M}$ ) and the average particle mass. It is nearly uniform in this region, but drops rapidly at its edge as the gas expands supersonically into its surroundings. The supersonic gas at some point passes through a reverse shock, and is re-thermalized to approximately the same temperature as within the wind injection region. The post-shock temperature of the gas is insensitive to the exact location of the shock. If the shock is very near to the edge of the injection region, the pre-shock gas will be only mildly supersonic. The relatively weak shock and, consequently, the relatively small temperature jump in this case are offset by the higher pre-shock temperature of the gas. However, if the shock occurs at a greater distance, then the pre-shock temperature of the wind may drop substantially lower, but its Mach number rises commensurably, and the kinetic energy per unit mass of this gas asymptotes to the original thermal energy per unit mass (ready to be thermalized again). If the reverse shock occurs inside the wind injection region, then the energy and mass within the region build (keeping the gas at the original temperature) until its pressure overcomes that of the surroundings.

Wind material density and energy density are added within the injection radius at each time-step such that their integrated rates over the volume are  $\dot{M}$  and  $(1/2)\dot{M}v_\infty^2$ , respectively. The rate of injected wind energy density is given by  $\dot{e}_w = (1/2)\dot{\rho}_w v_\infty^2$ , where  $\dot{\rho}_w$  is the rate of injected wind material density:

$$\dot{\rho}_w(\mathbf{r}) = \begin{cases} \frac{\dot{M}}{(4/3)\pi R_{\text{inj}}^3}, & \text{if } |\mathbf{r}| < R_{\text{inj}}; \\ 0, & \text{otherwise.} \end{cases} \quad (8)$$

Here,  $R_{\text{inj}}$  is the injection radius, which is given in Table 1 for each model.

We tested and confirmed that the evolution of a spherically symmetric wind-blown bubble in a neutral medium with no radiative cooling is as predicted using this method. The size of the injection region ( $\sim 10$  cells) in all our models was chosen to be large enough that the region is well resolved by the numerical grid and small enough that the injection region has little effect on the evolution of the bubble. An undesirable effect of this is that the injection radius is the radius the wind bubble starts with, so that the wind has had a head-start. It does, however, take time to inject enough pressure in the region to blow a wind. This is approximately the time it takes to add pressure into the injection region that is comparable to the ambient pressure, i.e.

$$t_{\text{start}} = \frac{p_i}{\dot{p}} = \frac{n_i k_B T_i (\gamma - 1)}{\dot{e}_w}, \quad (9)$$

where  $p_i$ ,  $n_i$  and  $T_i$  are the pressure, hydrogen number density and temperature of the ionized ambient gas, respectively,  $k_B$  is the Boltzmann constant and  $\gamma = 5/3$  is the ratio of heat capacities. The start times,  $t_{\text{start}}$ , are given in Table 1 for all the models.

## 2.5 Radiation field

Ionizing radiation from each star was assumed to be monochromatic. Non-ionizing far-ultraviolet radiation was also included to heat the gas in the same way as Henney et al. (2009). It was assumed that recombinations to the ground state of hydrogen are locally re-absorbed (i.e. the diffuse field was treated under the on-the-spot approximation). The recombination coefficient was therefore calculated using cubic spline interpolation of the case-B recombination coefficient data in Hummer (1994). Similarly, the collisional ionization of neutral hydrogen was calculated by cubic spline interpolation of the data in Raga, Mellema & Lundqvist (1997). The cross-

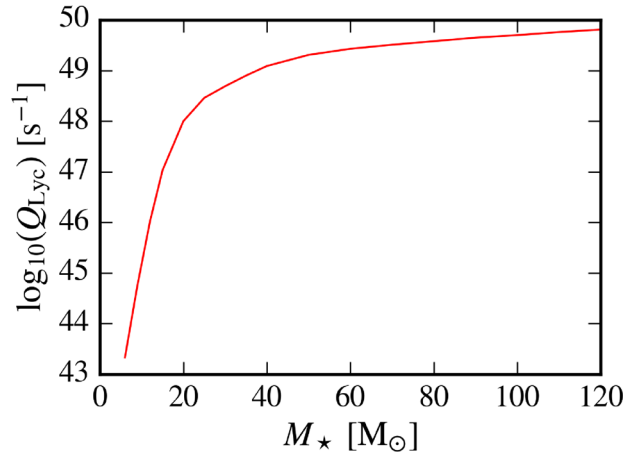


**Figure 3.** The Lyman continuum photon rate of stars plotted against stellar mass.

section for ionizing photons was taken from Osterbrock (1989). Fig. 3 shows the Lyman continuum flux plotted against stellar mass for our models.

## 3 RESULTS AND DISCUSSION

Plots of hydrogen number density, pressure, temperature and ionized hydrogen number density are given in Fig. 4 for a typical cometary H II region around a star with mass  $M_\star = 30 M_\odot$  at an age of  $t = 50$  kyr that starts the simulation in a local hydrogen number density of  $n_\star = 3.2 \times 10^4 \text{ cm}^{-3}$ . Nearest the star is the wind injection region of radius 0.04 pc from which a wind flows outwards becoming supersonic at its edge. The central temperature is  $\sim 10^8$  K and decreases outside of the injection radius to the wind reverse shock. Gas outside the injection region is accelerated to supersonic speeds. We refer to the gas between the wind injection region and the reverse shock as the ‘unshocked stellar wind region’. Downstream of the reverse shock is low-density shocked stellar wind material, which is at a uniform temperature of  $\sim 10^8$  K and subsonic. Further downstream lies the contact discontinuity separating the shocked stellar wind region and the cooler ( $\sim 8000$  K) ionized ambient gas. Earlier on in the evolution of this H II region, we would expect to see a shock ahead of the contact discontinuity, but pressures either side of the shock have equilibrated so that the shock no longer exists. Finally, the ionized region is bounded by an ionization front that separates the ionized gas from the neutral gas shock. Photo-ionization has heated the gas in the ionized region and therefore has created an over-pressure with respect to the surrounding ambient gas, which explains the presence of the shock just outside of the ionization front.

### 3.1 Ionization fronts

Assuming balance between photo-ionizations and recombinations, for a star in a uniform medium with no stellar wind, we have

$$Q_{\text{Lyc}} = \frac{4\pi}{3} n_i^2(t) \alpha_B R_{\text{IF}}^3(t), \quad (10)$$

where  $n_i$  is the hydrogen number density inside the ionized region,  $\alpha_B$  is the case-B recombination coefficient for hydrogen and  $R_{\text{IF}}(t)$

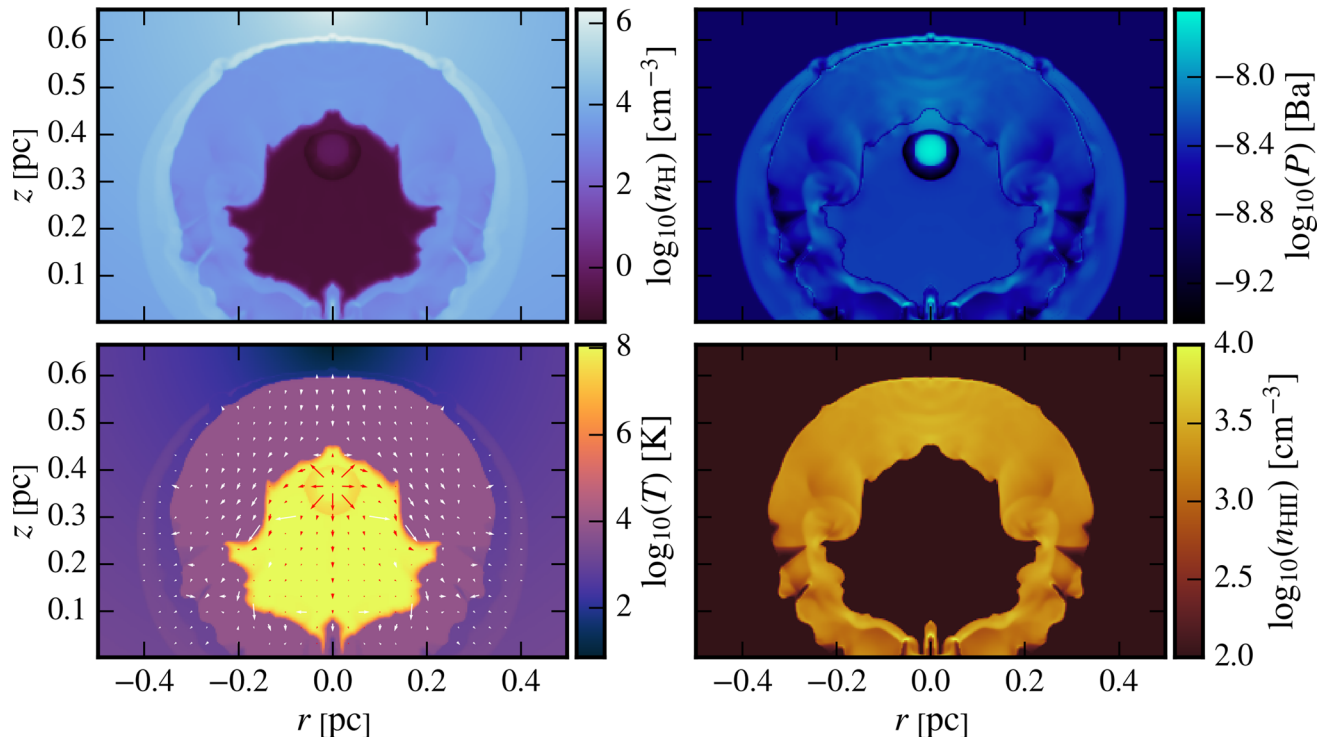


**Figure 4.** Maps of hydrogen number density (top left), pressure (top right), temperature (bottom left) and ionized hydrogen number density (bottom right) of a model H II region around a star of mass  $M_* = 30 M_\odot$  with a local hydrogen number density of  $n_* = 3.2 \times 10^4 \text{ cm}^{-3}$  at an age of  $t = 50 \text{ kyr}$ . The star is located at  $z = 0.37 \text{ pc}$  and  $r = 0 \text{ pc}$ . The blue arrows on the bottom-left plot represent velocities of  $3 < v \leq 30 \text{ km s}^{-1}$  and the red arrows represent velocities of  $30 < v \leq 2700 \text{ km s}^{-1}$ . The velocity vectors are separated by 10 cells in both dimensions.

is the time-dependent radius of the ionized region. The Strömgen radius is the initial radius of the ionized region,

$$R_{\text{st}} = \left( \frac{3Q_{\text{Lyc}}}{4\pi n_{\text{H}}^2 \alpha_{\text{B}}} \right)^{1/3}, \quad (11)$$

where  $n_{\text{H}}$  is the initial hydrogen number density of the uniform medium. Ionization heats the gas and sets up an over-pressure; expansion thereafter is driven by this over-pressure.

Raga, Cantó & Rodríguez (2012b) show that if the shock driven by the over-pressure is isothermal and it is assumed that the expanding H II region is in pressure balance with the shocked neutral gas, the equation of motion of the ionization front is

$$\frac{1}{c_i} \frac{dR_{\text{raga1}}(t)}{dt} = \left[ \frac{R_{\text{st}}}{R_{\text{raga1}}(t)} \right]^{3/4} - \frac{c_a^2}{c_i^2} \left[ \frac{R_{\text{st}}}{R_{\text{raga1}}(t)} \right]^{-3/4}. \quad (12)$$

The Spitzer approximation (Spitzer 1978) can be reproduced by this equation by noting that the second term on the right-hand side of equation is negligible at early times:

$$R_{\text{Spitzer}} = R_{\text{st}} \left( 1 + \frac{7t}{4t_s} \right)^{4/7}. \quad (13)$$

Here,  $t_s = R_{\text{st}}/c_i$  is the sound crossing time-scale and  $c_i$  is the sound speed of the ionized gas.

According to Raga, Cantó & Rodríguez (2012a), equation (12) neglects the inertia of the expanding neutral material and therefore derived solutions should underestimate the distance to the ionization front. Including the inertia gives the equation of the shell,

$$\frac{d^2 R_{\text{raga2}}(t)}{dt^2} + \frac{3}{R_{\text{raga2}}} \left[ \frac{dR_{\text{raga2}}(t)}{dt} \right]^2 = \frac{3R_{\text{st}}^{3/2} c_i^2}{R_{\text{raga2}}^{5/2}} - \frac{3c_a^2}{R_{\text{raga2}}}. \quad (14)$$

At early times, the solution can be approximated (Hosokawa & Inutsuka 2006) by

$$R_{\text{hi}} = R_{\text{st}} \left( 1 + \frac{7}{4} \sqrt{\frac{4t}{3t_s}} \right)^{4/7}. \quad (15)$$

Simulations of D-type expansion of ionization fronts (Bisbas et al. 2015) have shown close agreement with equation (15) at early times and with equation (12) at late times.

The sizes of the ionized regions simulated in the current paper are shown in Tables 3 and 4, along with the analytical radius of ionized regions that would evolve around stars with the same stellar parameters but in a uniform density medium (equation 12). The isothermal sound speed in the ionized ambient gas was assumed to be  $c_i = \sqrt{RT_i/\mu_{\text{H}}}$ , where the ionized gas temperature is  $T_i \simeq 8000 \text{ K}$ , the average molar mass of ionized hydrogen is  $\mu_{\text{H}} = 0.5 \text{ g mol}^{-1}$  and  $R$  is the gas constant, giving a sound speed of  $c_i = 11.5 \text{ km s}^{-1}$ . In Table 3, the measured ionization regions show a decrease in size for higher local densities, as expected. The sizes also increase for higher masses as a result of higher Lyman continuum photon fluxes. There is generally close agreement with the analytical radius, with the simulated regions consistently slightly larger. This is because of the contribution of the wind to driving the shock ahead of the ionization front. Simulations of stars without stellar winds confirm this as they produce H II regions with radii that are very close to those predicted by equation (12). For higher-mass stars, the radius of the simulated ionized region is noticeably larger than the analytical radius, suggesting that the strong winds from these stars are contributing relatively more to the expansion of the H II region.

**Table 3.** Measurements of  $D_i(\theta)$ , which is the distance from the star to the edge of the ionized region along a direction with polar angle  $\theta$ . The analytical ionization front radius,  $R_{\text{ragal}}$ , is also given by numerically solving equation (12). These measurements were made for stars of age of 50 kyr.

$M_*$ ( $M_\odot$ )	Dist. (pc)	$n_*$ ( $10^4 \text{ cm}^{-3}$ )				
		0.8	1.6	3.2	6.4	12.8
6	$D_i(0)$	0.034	0.019	0.010	0.0097	0.0056
	$D_i(\pi/2)$	0.037	0.023	0.014	0.010	0.0062
	$D_i(\pi)$	0.043	0.026	0.016	0.011	0.0076
	$R_{\text{ragal}}$	0.031	0.020	0.012	0.0078	0.0049
9	$D_i(0)$	0.078	0.053	0.039	0.021	0.014
	$D_i(\pi/2)$	0.085	0.060	0.039	0.023	0.014
	$D_i(\pi)$	0.106	0.071	0.042	0.025	0.015
	$R_{\text{ragal}}$	0.079	0.055	0.036	0.023	0.015
12	$D_i(0)$	0.15	0.095	0.077	0.062	0.035
	$D_i(\pi/2)$	0.17	0.12	0.088	0.062	0.040
	$D_i(\pi)$	0.19	0.15	0.11	0.071	0.045
	$R_{\text{ragal}}$	0.15	0.11	0.081	0.057	0.038
15	$D_i(0)$	0.20	0.16	0.14	0.093	0.070
	$D_i(\pi/2)$	0.26	0.20	0.15	0.11	0.079
	$D_i(\pi)$	0.31	0.24	0.18	0.13	0.096
	$R_{\text{ragal}}$	0.23	0.18	0.14	0.10	0.073
20	$D_i(0)$	0.26	0.24	0.19	0.17	0.13
	$D_i(\pi/2)$	0.40	0.32	0.24	0.19	0.15
	$D_i(\pi)$	0.48	0.38	0.30	0.22	0.17
	$R_{\text{ragal}}$	0.34	0.27	0.21	0.16	0.12
30	$D_i(0)$	0.30	0.26	0.23	0.21	0.18
	$D_i(\pi/2)$	0.56	0.43	0.34	0.26	0.21
	$D_i(\pi)$	0.78	0.58	0.42	0.34	0.24
	$R_{\text{ragal}}$	0.44	0.35	0.28	0.22	0.17
40	$D_i(0)$	0.31	0.30	0.26	0.24	0.20
	$D_i(\pi/2)$	0.74	0.56	0.44	0.34	0.26
	$D_i(\pi)$	1.07	0.75	0.56	0.47	0.33
	$R_{\text{ragal}}$	0.52	0.41	0.32	0.25	0.20
70	$D_i(0)$	0.33	0.32	0.33	0.26	0.24
	$D_i(\pi/2)$	1.19	0.87	0.77	0.48	0.39
	$D_i(\pi)$	1.38	1.03	0.88	0.60	0.47
	$R_{\text{ragal}}$	0.62	0.49	0.38	0.30	0.24
120	$D_i(0)$	1.33	0.39	0.39	0.32	0.28
	$D_i(\pi/2)$	1.96	1.25	1.14	0.71	0.54
	$D_i(\pi)$	2.35	1.57	1.34	0.88	0.75
	$R_{\text{ragal}}$	0.71	0.55	0.43	0.34	0.27

As a H II region expands, the pressure inside the region drops until it is equal to the ambient gas pressure, at which point it stagnates. The stagnation radius can be found, by setting  $dR_{\text{ragal}}(t)/dt = 0$  in equation (12), to be

$$R_{\text{stag}} = \left( \frac{c_i}{c_a} \right)^{4/3} R_{\text{st}}, \quad (16)$$

where  $c_a$  is the isothermal sound speed of the neutral ambient gas. The temperature of the neutral ambient gas is  $T_a \simeq 300$  K, so the sound speed is  $c_a \simeq 1.58 \text{ km s}^{-1}$ . In our models, therefore, we have  $R_{\text{stag}} \simeq 14.2R_{\text{st}}$ . Setting  $R_{\text{Spitzer}}(t_{\text{stag}}) = R_{\text{stag}}$  in equation (13), we can obtain an approximation for the stagnation time in terms of the sound-crossing time of the initial Strömgren sphere:  $t_{\text{stag}} \simeq 60t_s$ . We can see that for smaller Strömgren radii the stagnation time occurs earlier. Table 4 shows stagnating ionization fronts that occur at earlier ages for smaller-mass stars.

Most of the simulations of our models did not show the unbounded ionization front expansion predicted by Franco, Tenorio-

**Table 4.** Measurements of  $D_i(\theta)$ , which is the distance from the star to the edge of the ionized region along a direction with polar angle  $\theta$ . The analytical ionization front radius,  $R_{\text{ragal}}$ , is also given by numerically solving equation (12). These measurements were made for stars in a local number density of  $3.2 \times 10^4 \text{ cm}^{-3}$ .

$M_*$ ( $M_\odot$ )	Dist. (pc)	Age (kyr)				
		20	40	60	80	100
6	$D_i(0)$	0.015	0.012	0.012	0.016	0.014
	$D_i(\pi/2)$	0.016	0.014	0.015	0.016	0.016
	$D_i(\pi)$	0.019	0.015	0.019	0.019	0.018
	$R_{\text{ragal}}$	0.012	0.012	0.012	0.012	0.012
9	$D_i(0)$	0.038	0.041	0.041	0.038	0.038
	$D_i(\pi/2)$	0.036	0.041	0.040	0.039	0.038
	$D_i(\pi)$	0.041	0.043	0.043	0.039	0.050
	$R_{\text{ragal}}$	0.031	0.035	0.037	0.037	0.037
12	$D_i(0)$	0.059	0.078	0.085	0.092	0.096
	$D_i(\pi/2)$	0.069	0.087	0.097	0.103	0.107
	$D_i(\pi)$	0.079	0.110	0.120	0.121	0.125
	$R_{\text{ragal}}$	0.059	0.076	0.085	0.090	0.093
15	$D_i(0)$	0.11	0.13	0.15	0.17	0.18
	$D_i(\pi/2)$	0.11	0.15	0.17	0.19	0.21
	$D_i(\pi)$	0.12	0.16	0.19	0.23	0.25
	$R_{\text{ragal}}$	0.092	0.12	0.15	0.16	0.17
20	$D_i(0)$	0.13	0.18	0.21	0.24	0.26
	$D_i(\pi/2)$	0.15	0.22	0.26	0.30	0.33
	$D_i(\pi)$	0.17	0.24	0.31	0.35	0.40
	$R_{\text{ragal}}$	0.13	0.19	0.23	0.26	0.28
30	$D_i(0)$	0.17	0.21	0.24	0.26	0.29
	$D_i(\pi/2)$	0.21	0.30	0.36	0.43	0.47
	$D_i(\pi)$	0.24	0.38	0.45	0.50	0.63
	$R_{\text{ragal}}$	0.18	0.25	0.30	0.35	0.38
40	$D_i(0)$	0.19	0.24	0.26	0.29	0.31
	$D_i(\pi/2)$	0.26	0.24	0.47	0.54	0.61
	$D_i(\pi)$	0.31	0.47	0.59	0.73	0.82
	$R_{\text{ragal}}$	0.21	0.29	0.35	0.41	0.45
70	$D_i(0)$	0.24	0.34	0.29	0.34	0.34
	$D_i(\pi/2)$	0.36	0.67	0.81	1.00	1.15
	$D_i(\pi)$	0.50	0.70	0.87	0.95	1.07
	$R_{\text{ragal}}$	0.25	0.34	0.42	0.48	0.53
120	$D_i(0)$	0.32	0.40	0.44	0.42	0.48
	$D_i(\pi/2)$	0.70	0.96	1.16	1.27	1.46
	$D_i(\pi)$	0.81	1.25	1.32	1.51	1.59
	$R_{\text{ragal}}$	0.28	0.39	0.47	0.54	0.60

Table & Bodenheimer (1990) for  $\alpha > 3/2$ . Only for stars with masses  $M_* \geq 40 M_\odot$  and local densities  $n_* \leq 1.6 \times 10^4 \text{ cm}^{-3}$  did the ionization front break free of the cloud and almost always in finger-like structures (also known as the shadowing instability; see Williams 1999). In all other models, the regions are bounded approximately by a sphere, which is consistent with the three-dimensional simulations of off-centre UCH II regions by Mac Low et al. (2007). The regions are at a roughly constant density throughout the simulation and grow to a maximum radius that coincides with when the pressures either side of the ionization front have equalized.

These results very closely match those in Arthur (2007), in which the condition necessary for H II regions in power-law density environments to remain bounded during their initial formation stage was given by

$$\frac{1}{3} \gamma_{\text{sc}}^3 < \frac{2}{(2\alpha - 1)(2\alpha - 2)(2\alpha - 3)}, \quad (17)$$

**Table 5.** Measurements of  $D_s(\theta)$ , which is the distance from the star to the edge of the shocked stellar wind region along a direction with polar angle  $\theta$ . The analytical radius for a radiative bubble at the pressure confinement time  $R_p$  (see equations 20 and 18) is also given. These measurements were made for stars of age 50 kyr.

$M_\star$ ( $M_\odot$ )	Dist. (pc)	$n_\star$ ( $10^4 \text{ cm}^{-3}$ )				
		0.8	1.6	3.2	6.4	12.8
6	$D_s(0)$	0.0188	0.0097	0.0059	0.0062	0.0035
	$D_s(\pi/2)$	0.0243	0.0172	0.0088	0.0073	0.0043
	$D_s(\pi)$	0.0324	0.0176	0.0118	0.0093	0.0062
	$R_p$	0.0071	0.0050	0.0033	0.0027	0.0019
9	$D_s(0)$	0.0159	0.0243	0.0097	0.0035	0.0029
	$D_s(\pi/2)$	0.0150	0.0182	0.0170	0.0062	0.0037
	$D_s(\pi)$	0.0847	0.0176	0.0226	0.0141	0.0066
	$R_p$	0.0062	0.0047	0.0034	0.0023	0.0016
12	$D_s(0)$	0.041	0.011	0.022	0.021	0.012
	$D_s(\pi/2)$	0.037	0.022	0.025	0.022	0.018
	$D_s(\pi)$	0.142	0.112	0.063	0.038	0.021
	$R_p$	0.018	0.014	0.011	0.0083	0.0059
15	$D_s(0)$	0.031	0.044	0.040	0.026	0.022
	$D_s(\pi/2)$	0.051	0.044	0.040	0.031	0.020
	$D_s(\pi)$	0.216	0.159	0.119	0.082	0.066
	$R_p$	0.032	0.027	0.021	0.017	0.013
20	$D_s(0)$	0.040	0.047	0.057	0.065	0.043
	$D_s(\pi/2)$	0.079	0.074	0.062	0.057	0.050
	$D_s(\pi)$	0.344	0.259	0.191	0.138	0.113
	$R_p$	0.063	0.054	0.044	0.036	0.030
30	$D_s(0)$	0.074	0.079	0.079	0.071	0.071
	$D_s(\pi/2)$	0.15	0.14	0.13	0.13	0.14
	$D_s(\pi)$	0.65	0.38	0.36	0.25	0.17
	$R_p$	0.14	0.12	0.098	0.08	0.067
40	$D_s(0)$	0.13	0.11	0.15	0.12	0.094
	$D_s(\pi/2)$	0.28	0.24	0.18	0.27	0.18
	$D_s(\pi)$	0.94	0.62	0.44	0.40	0.29
	$R_p$	0.27	0.22	0.18	0.15	0.12
70	$D_s(0)$	0.22	0.21	0.22	0.18	0.18
	$D_s(\pi/2)$	1.08	0.79	0.63	0.43	0.37
	$D_s(\pi)$	1.12	0.91	0.77	0.56	0.47
	$R_p$	0.70	0.55	0.51	0.35	0.30
120	$D_s(0)$	1.18	0.34	0.31	0.25	0.22
	$D_s(\pi/2)$	1.88	1.18	1.06	0.63	0.49
	$D_s(\pi)$	2.19	1.52	1.26	0.81	0.71
	$R_p$	1.68	1.20	1.12	0.79	0.64

where  $y_{sc} = R_{st}/r_{sc}$  (i.e. the ratio of the Strömberg radius for a star in a uniform medium to the distance between the star and the cloud centre). Values of this ratio for each set of model parameters were calculated and are given in Table 1 by setting  $n_H$  in equation (11) equal to the local hydrogen number density,  $n_\star$ . Our power-law density environments have  $\alpha = 2$ , so equation (17) reduces to  $y_{sc} < 1$ , which is true for all our models. Arthur (2007) also found that in  $\alpha = 2$  power-law environments, if  $y_{sc} \lesssim 0.02$ , then pressure balance can halt the breakout of the H II region during the expansion stage. As mentioned before, the pressures do equalize before the H II regions can become unbounded for most models. However, this is also seen for models with  $y_{sc} > 0.02$ .

### 3.2 Shocked stellar wind region

Tables 5 and 6 list the sizes of the shocked stellar wind regions as a function of density and time, respectively. In Table 6, the sizes of the shocked stellar wind regions show a plateau at early times for

**Table 6.** Measurements of  $D_s(\theta)$ , which is the distance from the star to the edge of the shocked stellar wind region along a direction with polar angle  $\theta$ . The analytical radius for a radiative bubble at the pressure confinement time  $R_p$  (see equations 20 and 18) is also given. These measurements were made for stars in a local number density of  $3.2 \times 10^4 \text{ cm}^{-3}$ .

$M_\star$ ( $M_\odot$ )	Dist. (pc)	Age (kyr)				
		20	40	60	80	100
6	$D_s(0)$	0.0088	0.0062	0.0059	0.0094	0.0094
	$D_s(\pi/2)$	0.0112	0.0103	0.0103	0.0112	0.0112
	$D_s(\pi)$	0.0129	0.0098	0.0129	0.0124	0.0129
	$R_p$	0.0038	0.0035	0.0036	0.0039	0.0038
9	$D_s(0)$	0.0088	0.0106	0.0147	0.0106	0.0176
	$D_s(\pi/2)$	0.0103	0.0086	0.0118	0.0082	0.0088
	$D_s(\pi)$	0.0221	0.0265	0.0221	0.0071	0.0059
	$R_p$	0.0032	0.0036	0.0035	0.0034	0.0034
12	$D_s(0)$	0.018	0.013	0.028	0.022	0.044
	$D_s(\pi/2)$	0.016	0.018	0.021	0.028	0.028
	$D_s(\pi)$	0.050	0.078	0.053	0.081	0.066
	$R_p$	0.009	0.011	0.012	0.012	0.012
15	$D_s(0)$	0.041	0.038	0.035	0.042	0.048
	$D_s(\pi/2)$	0.033	0.038	0.041	0.039	0.044
	$D_s(\pi)$	0.049	0.099	0.141	0.176	0.191
	$R_p$	0.017	0.021	0.023	0.025	0.027
20	$D_s(0)$	0.035	0.059	0.057	0.044	0.047
	$D_s(\pi/2)$	0.041	0.059	0.081	0.065	0.059
	$D_s(\pi)$	0.106	0.184	0.229	0.283	0.329
	$R_p$	0.031	0.041	0.046	0.052	0.055
30	$D_s(0)$	0.092	0.071	0.079	0.088	0.074
	$D_s(\pi/2)$	0.088	0.100	0.119	0.118	0.118
	$D_s(\pi)$	0.184	0.329	0.371	0.412	0.515
	$R_p$	0.067	0.088	0.102	0.115	0.124
40	$D_s(0)$	0.12	0.15	0.15	0.11	0.14
	$D_s(\pi/2)$	0.21	0.18	0.21	0.21	0.26
	$D_s(\pi)$	0.28	0.41	0.41	0.65	0.73
	$R_p$	0.12	0.12	0.19	0.21	0.23
70	$D_s(0)$	0.18	0.22	0.19	0.20	0.23
	$D_s(\pi/2)$	0.32	0.56	0.70	0.64	0.71
	$D_s(\pi)$	0.47	0.70	0.81	0.88	1.07
	$R_p$	0.29	0.46	0.53	0.61	0.68
120	$D_s(0)$	0.32	0.29	0.26	0.33	0.37
	$D_s(\pi/2)$	0.36	0.90	1.06	1.22	1.38
	$D_s(\pi)$	0.58	1.14	1.32	1.41	1.59
	$R_p$	0.77	0.98	1.11	1.22	1.35

low-mass stars. The plateau occurs at later times for higher-mass stars. This suggests that the bubbles are becoming pressure-confined (plots of the pressure confirm this).

We use the results of an analysis of stellar wind evolution by Koo & McKee (1992) to see if this behaviour is physical. The terminal wind velocity in all of the models is lower than the critical wind velocity defined in Koo & McKee (1992, see their equation 2.5), indicating that the wind bubbles are radiative. In this regime, the cooling time of the shocked wind is shorter than the time it takes to accumulate a significant mass of gas ahead of the shock. We have found that the radii of the shocked stellar wind regions are consistent with pressure-confined fully radiative bubbles.

Numerical diffusion can cause extra cooling (i.e. the cooling length might not be sufficiently resolved and therefore intermediate temperatures are found in a higher volume of the gas). Kelvin–Helmholtz instabilities can also enhance cooling by increasing the surface area of the contact discontinuity. Increasing the resolution of the numerical grid increases the growth of these instabilities

to further enhance cooling. These behaviours are competing but overall the level of numerical diffusion has been found to decrease with higher resolution (Parkin & Pittard 2010). We carried out resolution tests that confirm that the cooling across the contact discontinuity was not enhanced significantly by numerical effects.

The shell radius for a radiative bubble is given by

$$R_{\text{shell}} = \left( \frac{3\mathcal{L}}{\pi\rho_i v_\infty} \right)^{1/4} t^{1/2}, \quad (18)$$

where  $\mathcal{L} = (1/2)\dot{M}v_\infty^2$  is the mechanical wind luminosity and  $\rho_i$  is the ionized ambient density. For stars with  $M_\star \geq 70 M_\odot$ , the wind is driving a shock that follows equation (18) just ahead of the ionization front, which explains why we are seeing large ionization front radii in Tables 3 and 4 for these stars. The shock ahead of the ionization front for the lower-mass stars evolves according to equation (12), indicating that the wind-blown bubble has been pressure-confined by the H II region.

A radiative bubble eventually becomes pressure-confined when the ram pressure of the shell is equal to the ambient pressure. Using equation (18), we can therefore obtain the time at which confinement occurs,

$$t_P = \left( \frac{3\mathcal{L}}{16\pi\rho_i c_1^4 v_\infty} \right)^{1/2}, \quad (19)$$

where  $c_1$  is the isothermal sound speed in the ionized ambient medium. The ionized ambient density,  $\rho_i$ , was determined for each snapshot as the density upstream of the shock in the ionized ambient region in the radial direction. Using equation (10), we can obtain an approximation for this density:

$$\rho_i = \left[ \frac{R_{\text{st}}}{D_i(\pi/2)} \right]^{3/2} \rho_\star. \quad (20)$$

Here,  $D_i(\pi/2)$  is the measured radial distance from star to ionization front given in Tables 3 and 4;  $D_i(\pi/2)$  gives an average value for the bubble radius.

For most of the models, the transition time is too short to be seen, either because the earliest data snapshot was taken at 2 kyr or because the bubble is small and therefore not well resolved. As a result, the bubbles quickly stall and consequently are missing the shock outside of the contact discontinuity that separates shocked stellar wind material and the ionized ambient medium. As the shock is missing and the wind-blown bubbles are behaving like radiative bubbles, the radial distance from the star to the contact discontinuity,  $D_s(\pi/2)$  in Tables 5 and 6, should be comparable to the analytical radius of the shock at the confinement time given in equation (19). The approximate final radius of the shocked wind region in the radial direction is

$$R_P = R_{\text{shell}}(t_P) = \left( \frac{3\mathcal{L}}{4\pi\rho_i c_1^2 v_\infty} \right)^{1/2}, \quad (21)$$

which is also given for each model in Tables 5 and 6. Looking at these tables, the measured transverse distances,  $D_s(\pi/2)$ , show closer agreement with the confinement radius,  $R_P$ , for higher-mass stars. In Tables 5 and 6, we can see generally better agreement for stars in lower-density environments and at later times, respectively. These results suggest that stars with high enough mass have stellar winds that dominate the expansion of the H II region. For lower-mass stars, the shocked stellar wind region is noticeably larger than predicted, suggesting that the expansion of the H II region is also contributing to the expansion of the shocked stellar wind region.

In all of the models, the contact discontinuity eventually stalls. For stars with mass  $6 \leq M_\star \leq 30 M_\odot$  in Table 6 the stellar wind

size in the transverse direction,  $D_s(\pi/2)$ , plateaus before they reach an age of 100 kyr. This behaviour is easily seen for the star with mass  $M_\star = 30 M_\odot$  but is harder to see for lower-mass stars because the contact discontinuity between the shocked stellar wind region and the ionized ambient region is unstable.

### 3.3 Emission measures

In order to see what our models would look like if the ionized region is optically thin, we calculated the emission measure:

$$EM = \int n_e^2 ds, \quad (22)$$

where  $n_e$  is the number density of free electrons and the integration is along a line of sight.

To perform this integration, we used the cylindrically symmetric ray-tracing scheme presented in the appendix of Dougherty et al. (2003). Grids of the resulting emission measures at a viewing projection angle of  $45^\circ$  are shown spanning two-dimensional parameter spaces in Figs 5 and 6. In Fig. 5, the effects of varying stellar mass and the star's local density were explored at a time of 50 kyr. The evolution over time of emission measures for different stellar masses is plotted in Fig. 6 at a local number density of  $n_\star = 3.2 \times 10^4 \text{ cm}^{-3}$ .

The figures clearly show two distinct behaviours. For stars with mass  $M_\star \leq 9 M_\odot$  (and also  $M_\star = 12 M_\odot$  for  $n_\star > 3.2 \times 10^4 \text{ cm}^{-3}$ ) the morphology of the cavity blown out by the stellar wind varies over the simulation time. In these models, the stellar wind is weak and is therefore isotropically confined by the H II region, explaining the non-cometary morphologies. A pressure gradient exists in these H II regions, which leads to the flow of material down the density gradient. Stars with higher mass have wind bubbles that are not confined down the density gradient, leading to expansion in this direction. These stars have cometary morphologies that do not change appreciably over a period of 200 kyr and show limb-brightening. Stars with masses  $M_\star \geq 70 M_\odot$  also show limb-brightening if  $n_\star > 3.2 \times 10^4 \text{ cm}^{-3}$ . The rest have H II regions that expand past the centre of the dense cloud so that this is the only feature picked up in the emission measure images. For the H II region in the bottom left of Fig. 5, we see limb-brightening because the high-density core is destroyed by the stellar wind.

For one of the models that does exhibit limb-brightening, we show in Fig. 7 the effects of changing the projection angle on the morphology. The projection angle is defined as

$$\theta_i = \arccos(\hat{z} \cdot \hat{d}), \quad (23)$$

where  $\hat{z}$  is a unit vector directed from star to cloud centre and  $\hat{d}$  is a unit vector directed from star to observer. At projection angles closer to  $90^\circ$ , limb-brightening is more pronounced (i.e. the ‘limbs’ wrap further around the centre of the object). Using the classification scheme of De Pree et al. (2005), the projected morphology is less cometary and more shell-like the closer the axis of symmetry of the H II region is oriented towards the observer. These results suggest that H II regions classified as having a shell-like morphology may be cometary viewed along their axis of symmetry (as noted by Mac Low et al. 1991).

### 3.4 Spectral indices

The change in specific intensity, at frequency  $\nu$ , across a ray segment in a grid cell is

$$\Delta I_\nu = (1 - e^{-\Delta\tau_\nu}) \left( \frac{j_\nu}{\alpha_\nu} - I_0 \right), \quad (24)$$

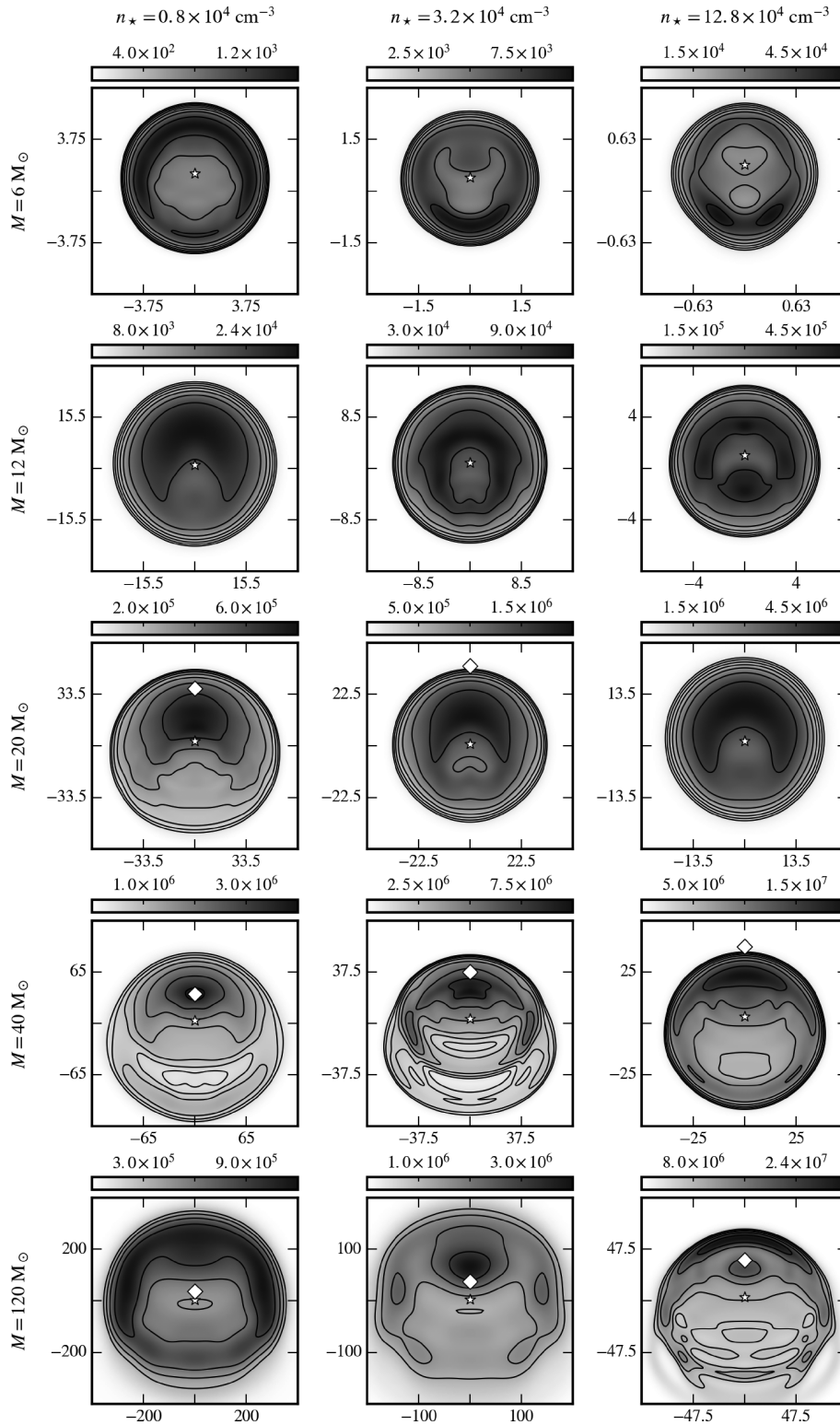


**Figure 5.** The emission measures (in  $\text{pc cm}^{-6}$ ) of simulated UCH II regions at an age of  $t = 50\,000$  yr and viewed at a projection angle (see equation (23)) of  $\theta_i = 45^\circ$ . Each row shows the emission measure for a star of a specified stellar mass (given on the far left) at increasing local number densities going right (number densities are given at the top of each column). The axes are in units of arcsec and the object is assumed to be at a distance of 1.5 kpc from the observer. Each map also shows logarithmic contours at  $\sqrt{2}$  intervals from the maximum emission measure. The star marker on each plot shows the position of the star and the diamond marker (where visible) shows the position of the cloud centre.

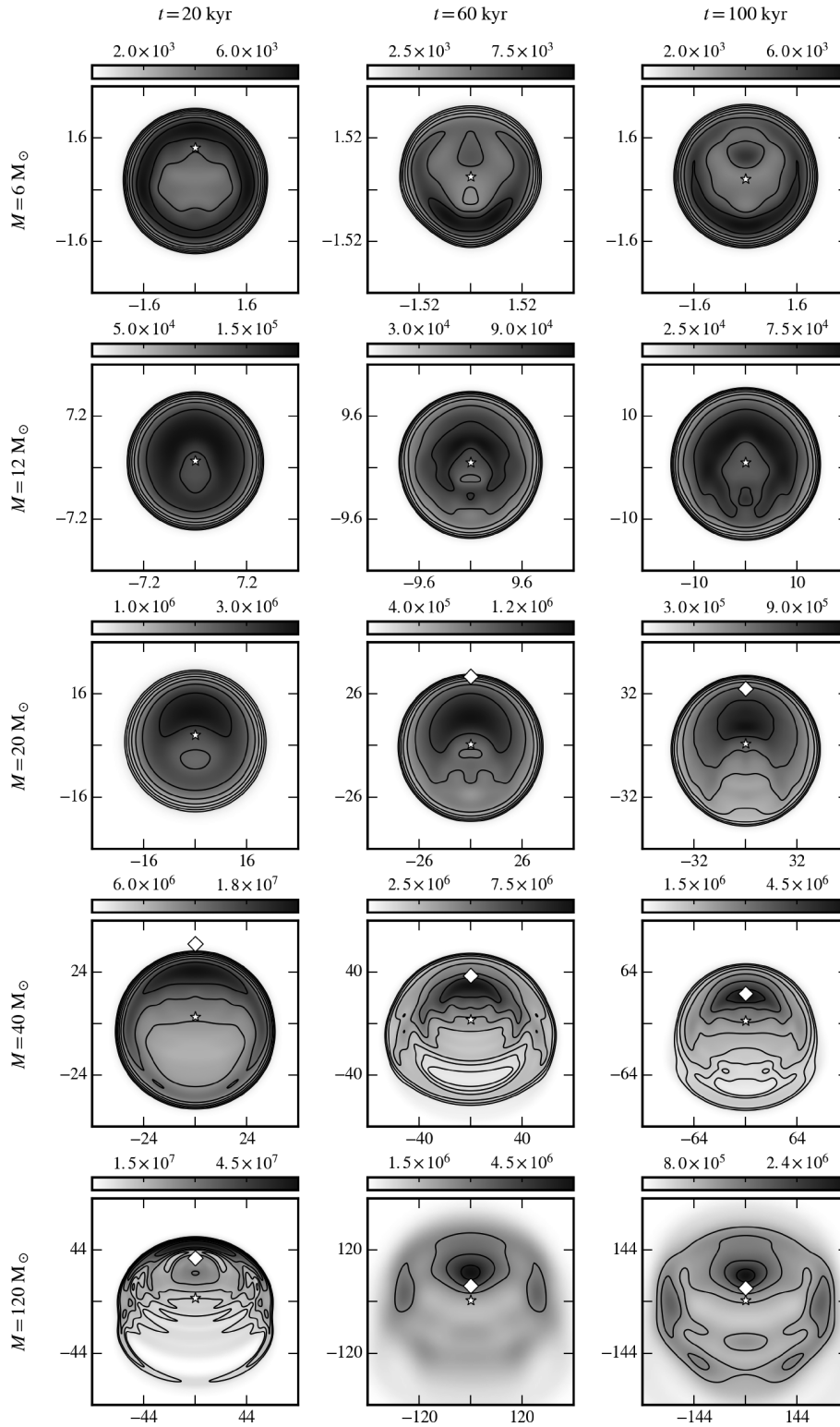


**Figure 6.** The emission measures (in  $\text{pc cm}^{-6}$ ) of simulated UCH II regions in a local hydrogen number density of  $n_{\star} = 3.2 \times 10^4 \text{ cm}^{-3}$  and viewed at a projection angle (see equation 23) of  $\theta_i = 45^\circ$ . Each row shows the emission measure for a star of a specified stellar mass (given on the far left) at increasing ages going right (age is given at the top of each column). The axes are in units of arcsec and the object is assumed to be at a distance of 1.5 kpc from the observer. Each map also shows logarithmic contours at  $\sqrt{2}$  intervals from the maximum emission measure. The star marker on each plot shows the position of the star and the diamond marker (where visible) shows the position of the cloud centre.

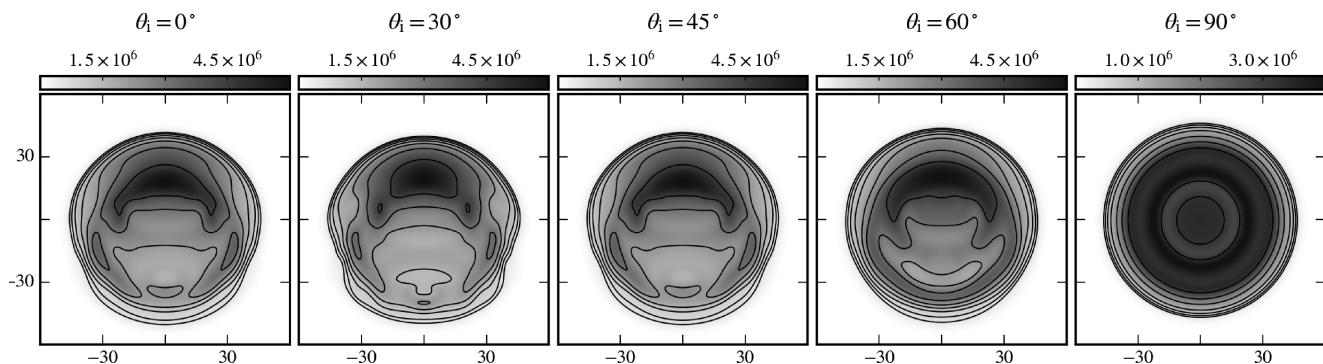


**Figure 7.** The emission measures (in  $\text{pc cm}^{-6}$ ) of a simulated H II region around a star with mass  $M_* = 30 M_\odot$  in a local hydrogen number density of  $n_* = 3.2 \times 10^4 \text{ cm}^{-3}$  at an age of  $t = 50 \text{ kyr}$  viewed at different projection angles (see equation 23), which are given at the top of each plot. The axes are in units of arcsec and the object is assumed to be at a distance of 1.5 kpc from the observer.

where  $I_0$  is the specific intensity at the start of the path segment,  $j_\nu$  and  $\alpha_\nu$  are the emission and absorption coefficients, respectively, and  $\Delta\tau_\nu$  is the optical depth across the segment given by

$$\Delta\tau_\nu = \alpha_\nu \Delta s, \quad (25)$$

where  $\Delta s$  is the path-length through the cell. The emission coefficient (Rybicki & Lightman 1979) is

$$j_\nu = \frac{32\pi q^6 k_e^3}{3m_e^{3/2} c^3} \sqrt{\frac{2\pi}{3k_B T}} Z^2 n_e n_i e^{-h\nu/k_B T} g_{\text{ff}}, \quad (26)$$

where  $q$  is the elementary charge,  $k_e$  is Coulomb constant,  $m_e$  is the mass of an electron,  $Z$  is the ionic charge,  $h$  is the Planck constant and  $g_{\text{ff}}$  is the velocity averaged Gaunt factor (Hummer 1988). Using the Kirchoff law,

$$j_\nu = \alpha_\nu B_\nu(T), \quad (27)$$

where  $B_\nu(T)$  is the Planck function, we have the absorption coefficient:

$$\alpha_\nu = \frac{16\pi q^6 k_e^3}{3m_e^{3/2} c h \nu^3} \sqrt{\frac{2\pi}{3k_B T}} Z^2 n_e n_i (1 - e^{-h\nu/k_B T}) g_{\text{ff}}. \quad (28)$$

We produced synthetic radio continuum maps by accumulating the changes in intensity along rays through the finite cells in our hydrodynamic solutions to pixels on an image plane. The flux density,  $S_\nu$ , in each pixel was obtained by integrating the intensity over the solid angle of the pixel. Spectral indices were approximated using the following maps,

$$\text{spectral index} = \frac{\partial \log S_\nu}{\partial \log \nu} \simeq \frac{\log S_{\nu_0} - \log S_{\nu_1}}{\log \nu_0 - \log \nu_1}, \quad (29)$$

where  $\nu_0$  and  $\nu_1$  are two closely separated frequencies.

A spectral index map for radio continuum emission is plotted in Fig. 8 for a star in the centre of the parameter space we are exploring for frequencies 1.4 and 5.0 GHz. Intermediate spectral indices (between  $-0.1$  and  $+2$ ) are found across the whole image. At the head and the limbs of the H II region, where the emission measure is highest, the spectral indices are higher ( $\sim 0.6$ ) than those in the cavity blown out by the stellar wind ( $\sim 0.2$ ).

Table 7 shows the spectral indices of models for a range of local densities and masses. These indices were calculated using the total radio continuum flux of each model for frequencies of 1.4 and 5.0 GHz. At these frequencies, the objects are more optically thick the higher the stellar mass (this is also seen in Table 8).

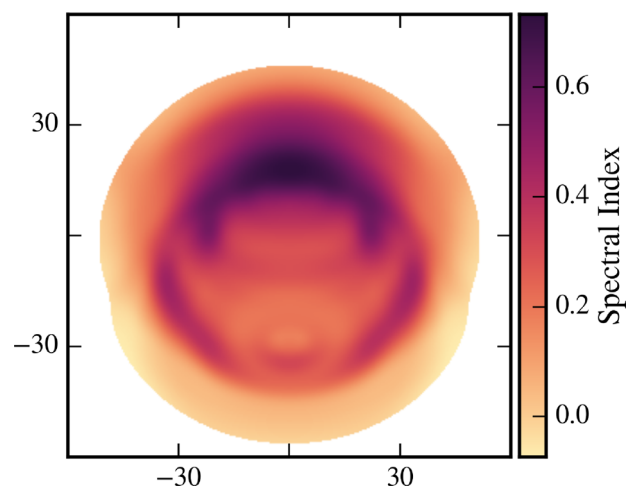


**Figure 8.** A spectral index map of radio continuum emission from a model H II region around a star of mass  $M_* = 30 M_\odot$  in a local hydrogen number density of  $n_* = 3.2 \times 10^4 \text{ cm}^{-3}$  and at an age of  $t = 50 \text{ kyr}$ . The object was viewed at a projection angle (see equation 23) of  $\theta_i = 45^\circ$ . Spectral indices for each pixel were calculated using two flux density images of the model for frequencies of 1.4 and 5.0 GHz. The axes are in units of arcsec and the object is assumed to be at a distance of 1.5 kpc from the observer. The region in white is below the noise level of the CORNISH survey ( $\sim 0.4 \text{ mJy beam}^{-1}$ ) and therefore a spectral index was not calculated. The integrated spectral index of this image is  $\alpha = 0.36$  (see Table 7).

**Table 7.** Spectral indices of model H II regions at an age of 50 kyr and viewing projection angle (see equation 23) of  $\theta_i = 45^\circ$ . The spectral indices were calculated using total fluxes for each model at frequencies of 1.4 and 5.0 GHz.

$M_*$ ( $M_\odot$ )	$n_*$ ( $10^4 \text{ cm}^{-3}$ )				
	0.8	1.6	3.2	6.4	12.8
6	-0.11	-0.11	-0.10	-0.10	-0.10
9	-0.10	-0.10	-0.10	-0.09	-0.07
12	-0.10	-0.10	-0.09	-0.07	-0.03
15	-0.09	-0.07	-0.05	-0.01	0.07
20	-0.03	0.02	0.10	0.21	0.38
30	0.08	0.20	0.36	0.56	0.83
40	0.15	0.30	0.49	0.76	1.04
70	0.12	0.30	0.36	0.78	1.08
120	0.04	0.16	0.27	0.66	1.05

**Table 8.** Spectral indices of model H II regions in a local hydrogen number density of  $n_* = 3.2 \times 10^4 \text{ cm}^{-3}$  and viewing projection angle (see equation 23) of  $\theta_i = 45^\circ$ .

$M_*$ ( $M_\odot$ )	Age (kyr)				
	20	40	60	80	100
6	-0.10	-0.10	-0.10	-0.10	-0.10
9	-0.10	-0.10	-0.10	-0.10	-0.10
12	-0.08	-0.09	-0.09	-0.09	-0.09
15	0.01	-0.04	-0.06	-0.07	-0.07
20	0.35	0.14	0.07	0.03	0.00
30	0.82	0.45	0.29	0.19	0.14
40	1.10	0.62	0.43	0.31	0.23
70	1.13	0.46	0.32	0.22	0.17
120	0.94	0.38	0.21	0.14	0.10

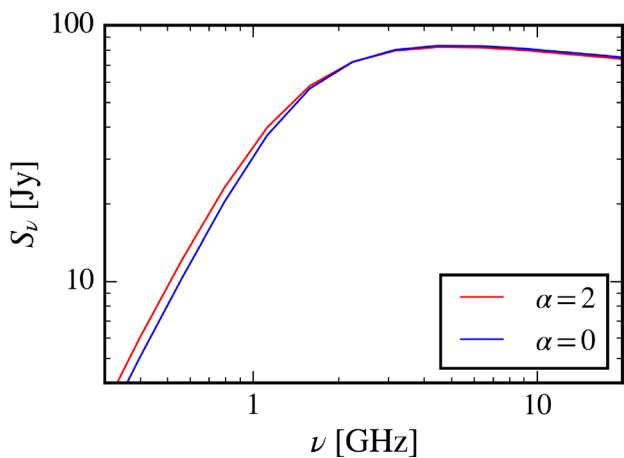


**Figure 9.** The radio spectrum of two model H II regions around stars of mass  $M_* = 30 M_\odot$  with a local hydrogen number density of  $n_* = 3.2 \times 10^4 \text{ cm}^{-3}$  at an age of  $t = 50 \text{ kyr}$  and at a projection angle (see equation 23) of  $\theta_i = 45^\circ$ . One of the stars is in a power-law density environment,  $\alpha = 2$ , and the other is in a uniform density environment,  $\alpha = 0$ . Both objects were viewed at a projection angle of  $\theta_i = 45^\circ$  and were assumed to be at a distance of 1.5 kpc.

Higher-mass stars have more intense ionizing radiation and blow stronger winds, so they ionize deeper into the dense cloud, leading to a higher proportion of the total flux from areas of high density. For masses  $M_* > 40 M_\odot$ , the spectral indices decrease, which is likely to be a result of the competing effect of larger regions having a higher proportion of flux from optically thin regions. These stars are ionizing the regions around the densest part of the cloud (or through it in the case of the star with  $M_* = 120 M_\odot$  in a local density of  $n_* = 12.8 \times 10^4 \text{ cm}^{-3}$ ).

In Table 8, spectral indices are shown to decrease over time. The density in a H II region decreases as it expands (after its initial Strömrgren expansion phase), so the spectral indices should also decrease.

Fig. 9 shows the radio spectrum of one of our model H II regions and also a H II region that is produced by the same star but in a uniform density environment. Surprisingly, the turn-over frequency is very similar for the power-law case, but it is slightly lower because the H II region covers more low-density gas down the slope than high-density gas up the slope. The total fluxes have a higher proportion from lower-density gas and therefore the integrated spectral indices will lean closer to indices from lower-density

regions. The close similarity between the spectral energy distributions is consistent with the fact that the density slope of ionized gas is much shallower than the initial slope in the neutral ambient gas.

### 3.5 Model limitations

If we had included the effects of the entire spectrum of radiation from our model stars, the temperature structures of our H II regions would be different. We would see higher temperatures near the ionization front because of the hardening of the radiation field (Wood & Mathis 2004). The extra pressure due to these high temperatures is expected to be  $\sim 20$  per cent higher than in our model H II regions.

Another limitation of our model is that we took the initial thermal pressure of the neutral gas to be uniform to prevent gas from moving away from the cloud centre (which would happen if the temperature was uniform instead). In a future study, the effects of gravity could be included to better model these environments.

Dust is an important factor in the evolution of high-density H II regions that we did not consider. Ionizing photons can be absorbed by dust and therefore dusty H II regions are expected to be smaller. Arthur et al. (2004) simulated dusty compact H II regions and found that the fraction of ionizing photons absorbed by dust decreases as the H II region expands, and so the effects of dust are less important in the later phases of expansion. They also found that dusty H II regions stagnate earlier than their dust-free counterparts.

## 4 CONCLUSIONS

We have simulated cometary H II regions that result from stars that blow stellar winds and are placed off-centre from a power-law density gas cloud. Models with stars of mass  $M_* \geq 12 M_\odot$  produce limb-brightening. Some are diminished if the star's H II region contains the dense centre of the cloud (which is true for stars with high Lyman output near low-density clouds). There is a cavity blown out by the stellar wind in each model, which is observed in real cometary H II regions. The morphological class of a H II region depends on the viewing projection angle. Morphologies are more shell-like the smaller the angle between the viewing direction and the object's axis of symmetry. Spectral indices are higher for higher-mass stars, which can be explained as larger H II regions covering more of the high-density gas near the cloud centre. This effect turns over at even higher masses as the volume of ionized low-density gas increases more than the volume of ionized high-density gas in the cloud centre. Model spectral energy distributions for power-law density models were almost identical to those of the same stars placed in uniform density surroundings, which is consistent with the shallow density structures we found in our simulated ionized regions. The turn-over frequency in the radio spectrum for our power-law density models is slightly lower compared to the models with uniform ambient density. This is because H II regions in a power-law density medium cover more low-density gas than high-density gas, which means that the proportion of emission from optically thin regions is higher.

In a subsequent paper, we will use the grid of simulated models presented in this paper to select H II regions that correspond to regions generated in a model Milky Way. The ultimate goal is to compare observables from this simulated survey with the CORNISH survey in order to investigate how well our models describe H II region evolution.

## ACKNOWLEDGEMENTS

We thank the anonymous reviewer for their critical reading of this paper and for their suggestions. This work was supported by the Science and Technology Facilities Council at the University of Leeds.

## REFERENCES

- Arquilla R., Goldsmith P. F., 1985, *ApJ*, 297, 436  
 Arthur S. J., 2007, *ApJ*, 670, 471  
 Arthur S. J., Hoare M. G., 2006, *ApJS*, 165, 283  
 Arthur S. J., Kurtz S. E., Franco J., Albarrán M. Y., 2004, *ApJ*, 608, 282  
 Bedijn P. J., Tenorio-Tagle G., 1981, *A&A*, 98, 85  
 Bisbas T. G. et al., 2015, *MNRAS*, 453, 1324  
 Bodenheimer P., Tenorio-Tagle G., Yorke H. W., 1979, *ApJ*, 233, 85  
 Castor J., McCray R., Weaver R., 1975, *ApJ*, 200, L107  
 Cesaroni R. et al., 2015, *A&A*, 579, A71  
 Chevalier R. A., Clegg A. W., 1985, *Nature*, 317, 44  
 Churchwell E., 2002, *ARA&A*, 40, 27  
 Comeron F., 1997, *A&A*, 326, 1195  
 Davies B., Hoare M. G., Lumsden S. L., Hosokawa T., Oudmaijer R. D., Urquhart J. S., Mottram J. C., Stead J., 2011, *MNRAS*, 416, 972  
 de Koter A., Schmutz W., Lamers H. J. G. L. M., 1993, *A&A*, 277, 561  
 de Koter A., Heap S. R., Hubeny I., 1997, *ApJ*, 477, 792  
 De Pree C. G., Wilner D. J., Deblasio J., Mercer A. J., Davis L. E., 2005, *ApJ*, 624, L101  
 Dougherty S. M., Pittard J. M., Kasian L., Coker R. F., Williams P. M., Lloyd H. M., 2003, *A&A*, 409, 217  
 Dyson J. E., Williams R. J. R., Redman M. P., 1995, *MNRAS*, 277, 700  
 Falle S. A. E. G., 1991, *MNRAS*, 250, 581  
 Felli M., Churchwell E., Massi M., 1984, *A&A*, 136, 53  
 Franco J., Tenorio-Tagle G., Bodenheimer P., 1990, *ApJ*, 349, 126  
 Franco J., García-Segura G., Kurtz S. E., Arthur S. J., 2007, *ApJ*, 660, 1296  
 Gaume R. A., Fey A. L., Claussen M. J., 1994, *ApJ*, 432, 648  
 Hatchell J., van der Tak F. F. S., 2003, *A&A*, 409, 589  
 Henney W. J., Arthur S. J., García-Díaz M. T., 2005, *ApJ*, 627, 813  
 Henney W. J., Arthur S. J., de Colle F., Mellema G., 2009, *MNRAS*, 398, 157  
 Hoare M. G., Kurtz S. E., Lizano S., Keto E., Hofner P., 2007, in Reipurth B., Jewitt D., Keil K., eds, *Protostars and Planets V*. Univ. of Arizona Press, Tucson, p. 181  
 Hoare M. G. et al., 2012, *PASP*, 124, 939  
 Hosokawa T., Inutsuka S.-i., 2006, *ApJ*, 646, 240  
 Hummer D. G., 1988, *ApJ*, 327, 477  
 Hummer D. G., 1994, *MNRAS*, 268, 109  
 Icke V., 1979a, *A&A*, 78, 352  
 Icke V., 1979b, *ApJ*, 234, 615  
 Icke V., Gatley I., Israel F. P., 1980, *ApJ*, 236, 808  
 Israel F. P., 1978, *A&A*, 70, 769  
 Koo B.-C., McKee C. F., 1992, *ApJ*, 388, 93  
 Korycansky D. G., 1992, *ApJ*, 398, 184  
 Kurtz S., Churchwell E., Wood D. O. S., 1994, *ApJS*, 91, 659  
 Lanz T., Hubeny I., 2007, *ApJS*, 169, 83  
 Liou M.-S., 2000, *J. Comput. Phys.*, 160, 623  
 Lumsden S. L., Hoare M. G., 1996, *ApJ*, 464, 272  
 Lumsden S. L., Hoare M. G., Urquhart J. S., Oudmaijer R. D., Davies B., Mottram J. C., Cooper H. D. B., Moore T. J. T., 2013, *ApJS*, 208, 11  
 Mac Low M.-M., van Buren D., Wood D. O. S., Churchwell E., 1991, *ApJ*, 369, 395  
 Mac Low M.-M., Toraskar J., Oishi J. S., Abel T., 2007, *ApJ*, 668, 980  
 Martins F., Schaerer D., Hillier D. J., 2005, *A&A*, 436, 1049  
 Mellema G., Iliev I. T., Alvarez M. A., Shapiro P. R., 2006, *New Astron.*, 11, 374  
 Meynet G., Maeder A., 2000, *A&A*, 361, 101  
 Mottram J. C. et al., 2011, *ApJ*, 730, L33  
 Nishikawa H., Kitamura K., 2008, *J. Comput. Phys.*, 227, 2560  
 Osterbrock D. E., 1989, *Astrophysics of Gaseous Nebulae and Active Galactic Nuclei*. Univ. Science Books, Mill Valley, CA  
 Parkin E. R., Pittard J. M., 2010, *MNRAS*, 406, 2373  
 Pirogov L. E., 2009, *Astron. Rep.*, 53, 1127  
 Purcell C. R. et al., 2013, *ApJS*, 205, 1  
 Quirk J. J., 1994, *Int. J. Numer. Methods Fluids*, 18, 555  
 Raga A. C., Mellema G., Lundqvist P., 1997, *ApJS*, 109, 517  
 Raga A. C., Cantó J., Rodríguez L. F., 2012a, *Rev. Mex. Astron. Astrofis.*, 48, 149  
 Raga A. C., Cantó J., Rodríguez L. F., 2012b, *MNRAS*, 419, L39  
 Redman M. P., Williams R. J. R., Dyson J. E., 1996, *MNRAS*, 280, 661  
 Reid M. J., Ho P. T. P., 1985, *ApJ*, 288, L17  
 Rodrigues O., 1840, *Journal de Mathématiques Pures et Appliquées*, 5, 380  
 Roe P. L., 1981, *J. Comput. Phys.*, 43, 357  
 Rozyczka M., 1985, *A&A*, 143, 59  
 Rybicki G. B., Lightman A. P., 1979, *Radiative Processes in Astrophysics*. Wiley-Interscience, New York  
 Spitzer L., 1978, *Physical Processes in the Interstellar Medium*. Wiley-Interscience, New York  
 Strang G., 1968, *SIAM J. Numer. Anal.*, 5, 506  
 Strickland D. K., Stevens I. R., 1998, *MNRAS*, 297, 747  
 Strömgren B., 1939, *ApJ*, 89, 526  
 Tenorio-Tagle G., Yorke H. W., Bodenheimer P., 1979, *A&A*, 80, 110  
 Tenorio-Tagle G., 1979, *A&A*, 71, 59  
 van Albada G. D., van Leer B., Roberts Jr. W. W. 1982, *A&A*, 108, 76  
 van Buren D., Mac Low M.-M., 1992, *ApJ*, 394, 534  
 van Buren D., Mac Low M.-M., Wood D. O. S., Churchwell E., 1990, *ApJ*, 353, 570  
 van der Tak F. F. S., van Dishoeck E. F., Evans II N. J., Blake G. A., 2000, *ApJ*, 537, 283  
 van Leer B., 1979, *J. Comput. Phys.*, 32, 101  
 Vink J. S., de Koter A., Lamers H. J. G. L. M., 1999, *A&A*, 350, 181  
 Vink J. S., de Koter A., Lamers H. J. G. L. M., 2000, *A&A*, 362, 295  
 Vink J. S., de Koter A., Lamers H. J. G. L. M., 2001, *A&A*, 369, 574  
 Vishniac E. T., 1983, *ApJ*, 274, 152  
 Walsh A. J., Burton M. G., Hyland A. R., Robinson G., 1998, *MNRAS*, 301, 640  
 Weaver R., McCray R., Castor J., Shapiro P., Moore R., 1977, *ApJ*, 218, 377  
 Whitworth A., 1979, *MNRAS*, 186, 59  
 Williams R. J. R., 1999, *MNRAS*, 310, 789  
 Williams R. J. R., Dyson J. E., Redman M. P., 1996, *MNRAS*, 280, 667  
 Wood D. O. S., Churchwell E., 1989a, *ApJS*, 69, 831  
 Wood D. O. S., Churchwell E., 1989b, *ApJ*, 340, 265  
 Wood K., Mathis J. S., 2004, *MNRAS*, 353, 1126  
 Yorke H. W., Tenorio-Tagle G., Bodenheimer P., 1983, *A&A*, 127, 313  
 Zhu F.-Y., Zhu Q.-F., Li J., Zhang J.-S., Wang J.-Z., 2015, *ApJ*, 812, 87

## APPENDIX A: CODE TESTS

## A1 R-type expansion and shadowing

Two tests were carried out to ensure the accuracy of the radiative transfer scheme. The first test compares the radius of a simulated Strömgren sphere with the analytical solution for the Strömgren radius (Strömgren 1939):

$$R_{\text{st}} = \left( \frac{3Q_{\text{Lyc}}}{4\pi n_{\text{H}}^2 \alpha_{\text{B}}} \right)^{1/3} (1 - e^{-t/t_{\text{rec}}})^{1/3}. \quad (\text{A1})$$

where  $t_{\text{rec}} = 1/n_{\text{H}}\alpha_{\text{B}}$  is the recombination time. We assume here that  $Q_{\text{Lyc}} = 10^{48}$  photons  $\text{s}^{-1}$ ,  $n_{\text{H}} = 100 \text{ cm}^{-3}$ , and  $\alpha_{\text{B}} = 2.59 \times 10^{-13} \text{ cm}^3 \text{ s}^{-1}$ .

The results of this test are shown in Fig. A1 along with a comparison between first-order and second-order explicit schemes

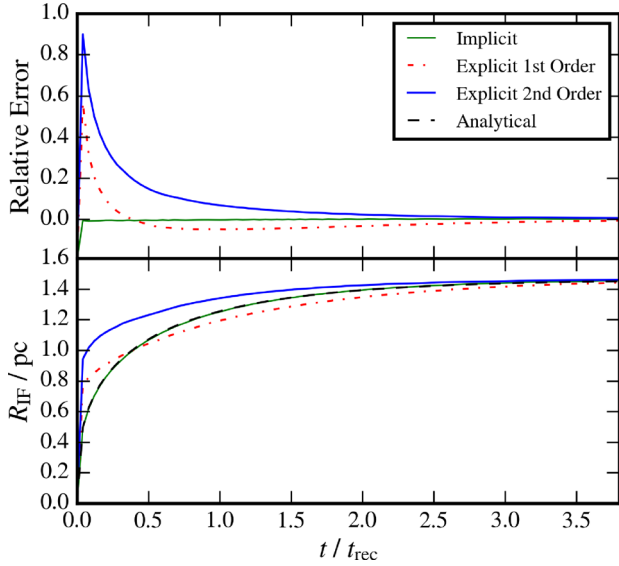


**Figure A1.** Expansion of a H II region as a function of time in a uniform density environment. There is no coupling to the hydrodynamics. The dashed black curve represents the analytical solution, which is partially obscured by the solid green curve (simulated with the implicit scheme). The ionization fronts simulated by explicit first-order and second-order schemes are shown by the dash-dotted red curve and the thick solid blue curve, respectively.

and the implicit scheme TORCH uses. Clearly, the implicit scheme outperforms the other schemes, converging to the analytical solution in a time much smaller than the recombination time.

Simulations of UCH II regions with stellar winds should show trapping of the ionization front behind the swept-up wind bubble. To see if the code works accurately in such a situation, the Strömgen sphere test was repeated but with a dense square clump positioned near the ionizing source. The clump effectively blocks photo-ionizing radiation from propagating into the ‘shadow’ region. However, there is some numerical diffusion into the shadow region because of the interpolative nature of the short-characteristics ray-tracing scheme. This will have a negligible effect on the dynamics of any simulated H II region. Fig. A2 shows the evolution of the ionized H II fraction in the shadow test.

## A2 D-type expansion

TORCH was benchmarked against the results of the one-dimensional spherically symmetric D-type expansion tests of Bisbas et al. (2015). The early- and late-phase simulations, described by this author, of D-type ionization front expansion into an initially uniform density ( $\rho_{\text{H}} = 5.21 \times 10^{-21} \text{ g cm}^{-3}$ ) isothermal gas were run. The ionizing star in this simulation has a Lyman continuum photon rate of  $Q_{\text{Ly}\alpha} = 10^{49} \text{ photons s}^{-1}$ , which produces an initial Strömgen sphere of radius  $R_{\text{st}} = 0.314 \text{ pc}$  and temperature  $T_{\text{HII}} = 10\,000 \text{ K}$ . The temperature of the neutral ambient medium was set to  $T_{\text{HI}} = 100 \text{ K}$  for the early phase and to  $T_{\text{HI}} = 1000 \text{ K}$  for the late phase. Coupling between gas and radiation physics was achieved for an isothermal equation of state by setting the temperature of a gas element according to the ionized fraction of hydrogen in that element:

$$T = T_{\text{HI}} + (T_{\text{HII}} - T_{\text{HI}})f_{\text{HII}}. \quad (\text{A3})$$

Here,  $T_{\text{HI}}$  is the temperature of fully neutral hydrogen and  $T_{\text{HII}}$  is the temperature of fully ionized hydrogen.

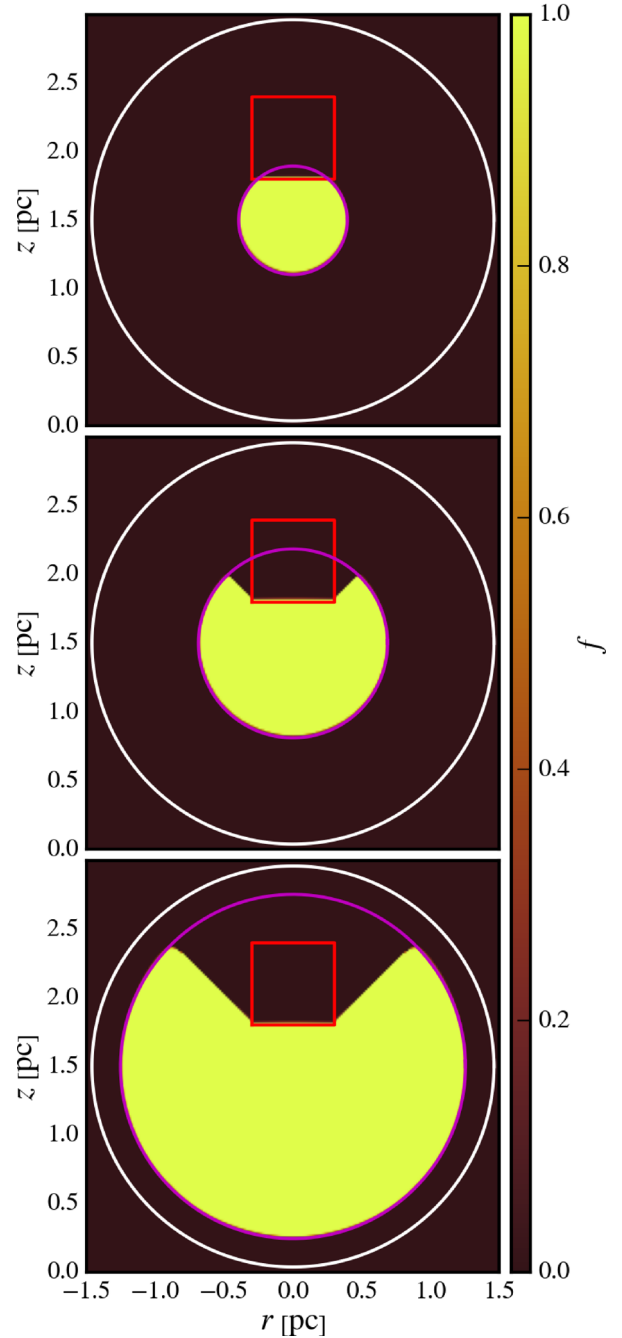


**Figure A2.** H II fraction evolution in a uniform density medium with a dense square clump (in red) nearby. The magenta circle traces the analytical Strömgen sphere, which approaches the white circle as  $t \rightarrow \infty$ . The snapshots were taken at 24 yr (top), 135 yr (middle) and 1224 yr (bottom). The star was positioned at (0 pc, 1.5 pc) and the centre of the square clump (of side-length 0.6 pc) was positioned at (0 pc, 2.1 pc).

Early on in the evolution (a few recombination times) a weak-R ionization front expands according to equation (A1). The gas is heated so that the ionized region is over-pressured with respect to the neutral gas. As the ionization front slows down, it becomes R-critical; the pressure wave overtakes the front and steepens into a shock wave, compressing the gas behind it. The R-critical ionization front transitions into a D-critical front with an isothermal shock ahead of it. D-type expansion is then driven by the over-pressure on the sound crossing time-scale  $t_s = R_{\text{st}}/c_i$ , where  $R_{\text{st}}$  is the Strömgen

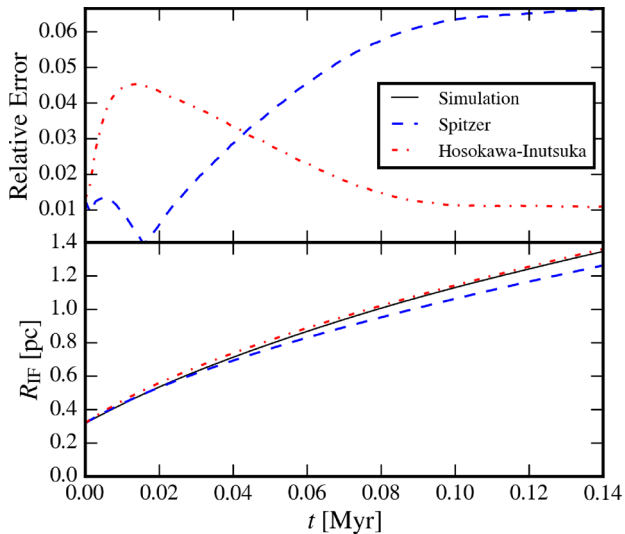


**Figure A3.** The one-dimensional simulation results (using 2000 cells) of the early-phase expansion of a H II region in a uniform density environment described in Appendix A2. The solid black curve shows the simulated ionization front radius. The Spitzer (equation 13) and Hosokawa–Inutsuka (equation 15) solutions are given by the dashed blue curve and dash-dotted red curve, respectively.

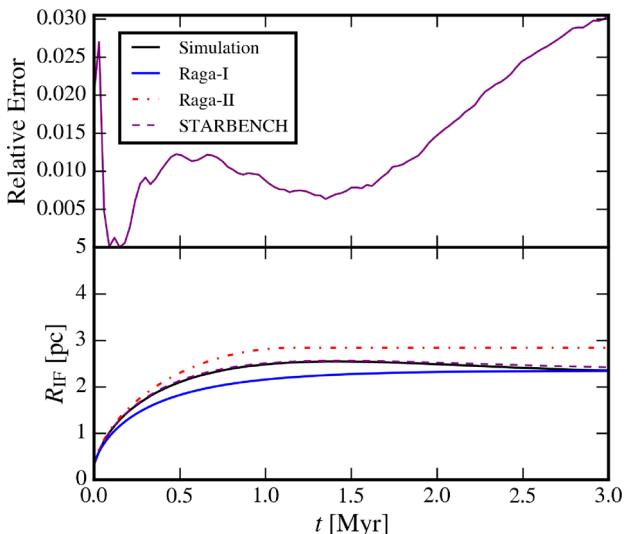


**Figure A4.** The one-dimensional simulation results (using 2000 cells) of the late-phase expansion of a H II region in a uniform density environment described in Appendix A2. The solid black curve shows the simulated ionization front radius. The analytical radii labelled Raga-I (thick solid blue curve) and Raga-II (dash-dotted red curve) show the analytical radii predicted by equations (12) and (14), respectively.

radius given in equation (A1) and  $c_1 = 12.85 \text{ km s}^{-1}$  is the sound speed of the ionized gas. Fig. A3 shows the expansion of the ionization front in the early phase. The expansion begins by following the Spitzer solution (equation 13) and eventually follows the solution by Hosokawa & Inutsuka (2006) (equation 15). In Fig. A4, we show the ionization front evolution in the late phase. The simulated front is a close fit to the STARBENCH equation (Bisbas et al. 2015), with an error of less than 3 per cent for the simulation duration.

### A3 Wind-blown bubble

The wind-blown bubble model of Strickland & Stevens (1998) was simulated using TORCH to test if the cooling instability in the shell is reproduced. A stellar wind with mass-loss rate  $\dot{M}_W = 5 \times 10^{-5} M_\odot \text{ yr}^{-1}$  and terminal wind speed  $v_W = 2000 \text{ km s}^{-1}$  was modelled by including source terms  $\dot{\rho}_W$  and  $\dot{e}_W$  within a radius of 10 grid cells (see Section 2.4).

As was found in Strickland & Stevens (1998), the wind sweeps material into a shock-heated shell. The shell starts out thick, but rapidly cools and collapses as it grows. Eventually, the shell is so thin that it becomes unstable to thin shell and Vishniac instabilities (Vishniac 1983). The evolution of the ionized hydrogen number density during the simulation is shown in Fig. A5 and agrees well with the model in Strickland & Stevens (1998).

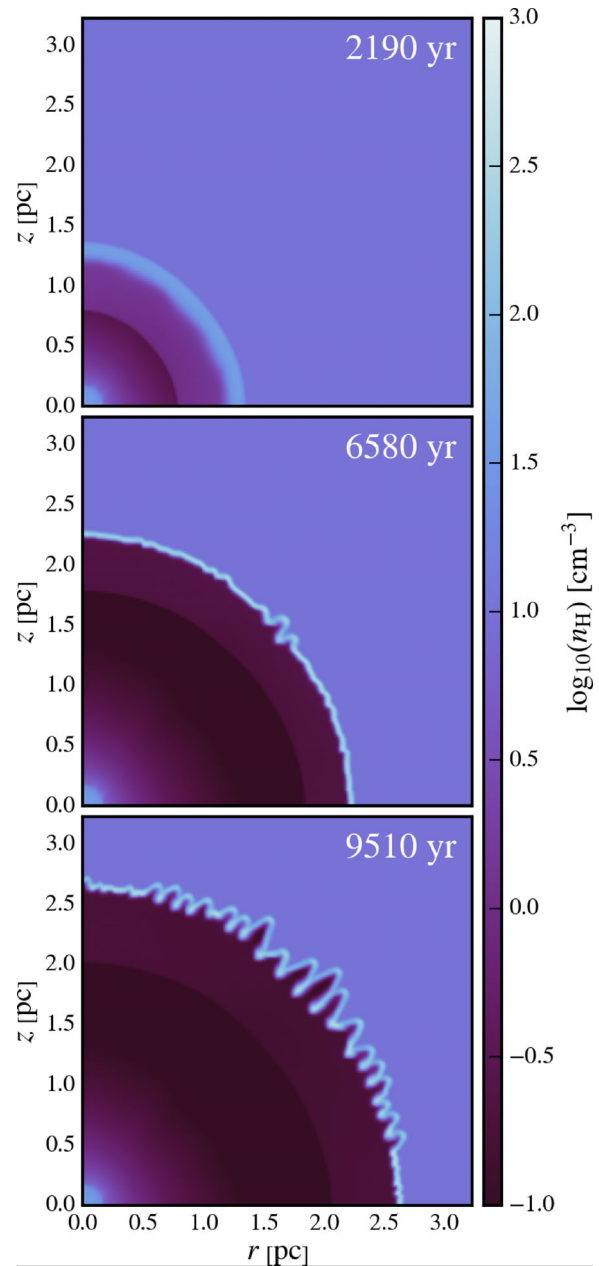


**Figure A5.** Snapshots of  $\log_{10}$  of the hydrogen number density  $n_H$  taken during a simulation of a wind-blown bubble.

#### A4 Shadowing instability

This final test utilizes both the radiation and cooling modules in order to reproduce the shadowing instability (Williams 1999). A wind was set up in the same way as in Section 2.4 with wind, star and initial gas parameters taken from the shadowing instability test in Arthur & Hoare (2006). If the cooling time is too short, the dense swept-up shell can collapse while the effects of the staggered grid are still appreciable (i.e. the shell has a low resolution). For this reason, the energy flux from the heating and cooling module was artificially reduced by a factor of 100 in order to increase the cooling length and so delay the onset of the cooling instability.

Fig. A6 shows the evolution of the ionized gas density (similar to fig. 2 in Arthur & Hoare 2006), which behaves as expected. The

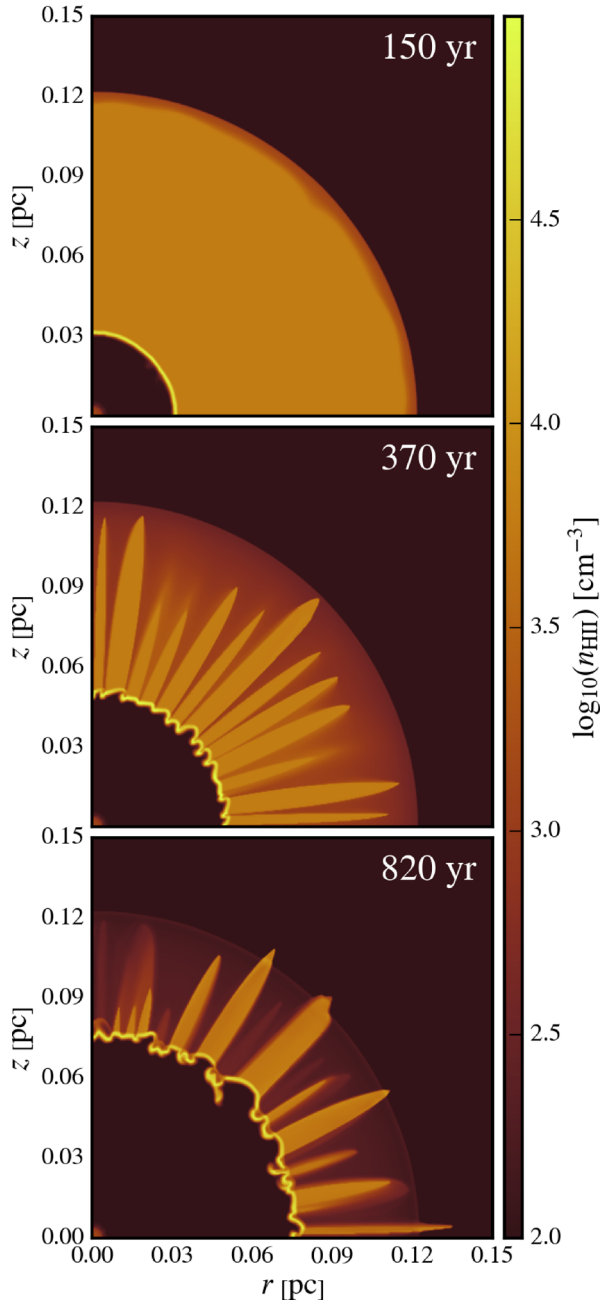


**Figure A6.** Snapshots of  $\log_{10}$  of the ionized hydrogen number density  $n_{\text{H}}$  taken during a simulation of a photo-ionized wind-blown bubble.

cooling instability discussed in Appendix A3 occurs and produces a variation in the optical depth, leading to the tell-tale spokes of the shadowing instability.

#### APPENDIX B: ROTATED-HYBRID HLL/HLLC

To solve the Riemann problem across inter-cell boundaries we first implemented a HLLC Riemann solver. After testing, it was apparent that this scheme is not robust as unacceptable flow fields can result called carbuncle instabilities (Quirk 1994). Schemes such as HLL and Rusanov do not have this problem as they are highly dissipative. There are a few ways to cure schemes that are prone to the carbuncle phenomenon; the technique we decided to use was to combine HLL and HLLC schemes into a rotated-hybrid Riemann solver (Nishikawa & Kitamura 2008).

The scheme starts by decomposing the geometric grid cell face normal  $\mathbf{n}$  into two orthogonal directions:

$$\mathbf{n}_1 = \begin{cases} \frac{\Delta \mathbf{q}}{|\Delta \mathbf{q}|}, & \text{if } |\Delta \mathbf{q}| > \epsilon, \\ \mathbf{n}_\perp, & \text{otherwise;} \end{cases} \quad (\text{B1})$$

$$\mathbf{n}_2 = \frac{(\mathbf{n}_1 \times \mathbf{n}) \times \mathbf{n}_1}{|(\mathbf{n}_1 \times \mathbf{n}) \times \mathbf{n}_1|}. \quad (\text{B2})$$

Here,  $\Delta \mathbf{q} = (u_{\text{R}} - u_{\text{L}}, v_{\text{R}} - v_{\text{L}})$  is the velocity difference vector,  $\mathbf{n}_\perp$  is a direction tangent to the geometric face and  $\epsilon$  is a small number. The second case in equation (B1) ensures that only the HLLC solver is used when streamwise velocity fields are smoothly varying; only at discontinuities will the HLL solver be applied. The flux across this grid cell face is

$$\mathbf{F} = \mathbf{n} \cdot \mathbf{n}_1 \mathbf{F}_{\text{HLL}}(\mathbf{n}_1) + \mathbf{n} \cdot \mathbf{n}_2 \mathbf{F}_{\text{HLLC}}(\mathbf{n}_2). \quad (\text{B3})$$

Fluxes  $\mathbf{F}_{\text{HLL}}(\mathbf{n}_1)$  and  $\mathbf{F}_{\text{HLLC}}(\mathbf{n}_2)$  are calculated by first finding the velocity in a new coordinate system:

$$\mathbf{v}' = \mathbf{R} \mathbf{v}, \quad (\text{B4})$$

where  $\mathbf{v}$  is the velocity in the original coordinate system on either the left or the right side of the cell interface and  $\mathbf{R}$  is the rotation matrix (defined as rotating decomposed Riemann problem directions,  $\mathbf{n}_1$  or  $\mathbf{n}_2$ , to align with the geometric cell face normal,  $\mathbf{n}$ ).

Using the rotation formula of Rodrigues (1840), the rotation matrix  $\mathbf{R}$ , which rotates unit vector  $\mathbf{n}_i$  on to unit vector  $\mathbf{n}$ , is given by

$$\mathbf{R} = \mathbf{I} + [\mathbf{w}]_\times + \frac{1-c}{s^2} [\mathbf{w}]_\times^2, \quad (\text{B5})$$

where

$$\mathbf{w} = \mathbf{n}_i \times \mathbf{n}, \quad (\text{B6})$$

$$c = \mathbf{n}_i \cdot \mathbf{n}, \quad (\text{B7})$$

$$s = \|\mathbf{w}\|, \quad (\text{B8})$$

and  $[\mathbf{w}]_\times$  is the skew-symmetric cross-product matrix of  $\mathbf{w}$ ,

$$[\mathbf{w}]_\times = \begin{pmatrix} 0 & -w_3 & w_2 \\ w_3 & 0 & -w_1 \\ -w_2 & w_1 & 0 \end{pmatrix}. \quad (\text{B9})$$

With rotated left and right Riemann states for each decomposed Riemann direction, we can now solve the one-dimensional Riemann problem. Solving these problems leaves us with momentum fluxes

$L'$  (calculated using  $v'$ ) that need to be rotated back on to the original coordinate system:

$$\mathbf{L} = \mathbf{R}^{-1} \mathbf{L}'. \quad (\text{B10})$$

Along with the rest of the flux components, this gives us  $\mathbf{F}_{\text{HLL}}(\mathbf{n}_1)$  and  $\mathbf{F}_{\text{HLLC}}(\mathbf{n}_2)$ . Using the rotated Riemann solver effectively applies the HLL solver in the direction normal to shocks (suppressing the carbuncle instability) and applies the HLLC solver across shear layers in order to minimize dissipation.

Liou (2000) argues that intermediate cells across a shock exchange information transversely to their neighbours along the shock, which can develop into a carbuncle instability. Considering a face connecting two neighbouring intermediate cells, any

significant perturbation travelling in a direction normal to this face will lead to a velocity difference vector oriented in the same direction (Nishikawa & Kitamura 2008). This means that the HLL Riemann solver will introduce dissipation in this direction, suppressing the instability. The resulting scheme pays for its robustness with an acceptable drop in accuracy (using a dissipative Riemann solver) and speed (using two Riemann solvers).

This paper has been typeset from a  $\text{\TeX}/\text{\LaTeX}$  file prepared by the author.